PREFERENTIAL OXIDATION OF H_2 - CH_4 MIXTURES ON NICKEL-SILICA BASED CORE-SHELL CATALYSTS

by

Yahui Yang

B.S. in Chemical Engineering, East China University of Science and Technology, 2013

Submitted to the Graduate Faculty of

Swanson School of Engineering in partial fulfillment

of the requirements for the degree of

Master of Science

University of Pittsburgh

2015

UNIVERSITY OF PITTSBURGH

SWANSON SCHOOL OF ENGINEERING

This thesis was presented

by

Yahui Yang

It was defended on

March 26, 2015

and approved by

Robert M. Enick., Ph.D., Professor, Department of Chemical and Petroleum Engineering

Giannis Mpourmpakis, Ph.D., Assistant Professor, Department of Chemical and Petroleum Engineering

Thesis Advisor: Götz Veser, Ph.D., Professor, Department of Chemical and Petroleum Engineering

PREFERENTIAL OXIDATION OF H_2 - CH_4 MIXTURES ON NICKEL-SILICA BASED CORE-SHELL CATALYSTS

Yahui Yang, M.S.

University of Pittsburgh, 2015

Core-shell nanostructures have drawn a lot of attention thanks to their ability to isolate the nanoparticle cores inside the support and hence alleviate sintering problem. Metal-silica core-shell materials are among the most typical core-shell nanostructures. Considering the porosity of the silica shell, the silica layer in such metal-silica core-shell materials also could serve as a porous membrane for preferential diffusion of different molecules.

In the present work, we aim to apply this to H_2 - CH_4 mixtures, where we expect a preferential diffusion of H_2 through the silica layer and hence a preferential conversion of H_2 over the metal cores inside the silica shell.

Two core-shell materials with different configuration were synthesized to investigate the impact of nanostructure on the diffusion of H_2 and CH_4. These two materials are non-hollow $Ni@SiO_2$ (denoted as $nhNi@SiO_2$) where Ni nanoclusters are evenly dispersed in a porous silica nanoparticle, and hollow $Ni@SiO_2$ (denoted as $hNi@SiO_2$) where Ni nanoclusters decorate the inside wall of a pronounced cavity enclosed by a porous silica shell. A conventional $Ni\text{-}SiO_2$ catalyst (where nickel nanoclusters are dispersed on external silica surface) was synthesized as a comparison.

In unmixed H_2 and CH_4 oxidation tests, we find the expected impact of diffusion through the porous silica shell on the conversion of H_2 and CH_4 with nickel oxide, suggesting that these materials might allow for selective conversion. Different diffusion pathway in these two

materials results in different kinetics. In co-fed tests, H_2 conversion curve precedes CH_4 conversion on both materials, and this is more pronounced on hollow material, suggesting H_2 diffuses more easily than CH_4 and a shell with uniform diffusion distance can result in selectivity. It is hence expected to see the “selective” diffusion enhanced with an increased silica shell thickness.

Our future work will focus on hNi@SiO_2 with thicker silica shell. Furthermore, we will investigate the preferential oxidation of hydrogen versus ethane, propane, or heavier hydrocarbon for which we expect the selective diffusion of hydrogen versus other hydrocarbons to be further enhanced as the difference in molecular weight between the hydrocarbon and hydrogen—and hence the difference in diffusion coefficient—become larger. Ultimately, we aim to apply these metal-silica core-shell materials to selective dehydrogenation reactions to remove the produced hydrogen from the product mixture.

TABLE OF CONTENTS

LIST OF TABLES

LIST OF FIGURES

PREFACE

First, I would like to thank my advisor Dr. Götz Veser for his generous support and detailed guidance in my work. You lead me patiently and systematically to think as an academic researcher. I benefit a lot from the way you work. It has been an absolutely a great pleasure to learn and work with you.

Then, I would like to thank my lab mates Yungchieh, Sharlee, Hao and Amey for helping me and sharing beneficial experience with me. Especially thank Yungchieh for instructing me to use many instruments in lab and thank Sharlee for helping me doing TEM for my samples. We had a good time together in lab, which I will cherish forever.

Furthermore, I would like to thank the faculty, staff and students of the Chemical Engineering Department at the University of Pittsburgh for their friendly help.

Finally, I would like to thank me parents. Thank you for your constant support and inclusion so that I can do what I want. Without you, I cannot make this. Love you.

1.0 INTRODUCTION

Core-shell nanomaterials have many practical applications in the biomedical, electronics as well as catalytic fields [1]. In particular, the emergence of core-shell nanostructures has significant implications in catalysis. The outer shells can isolate the catalytically active nanoparticle cores and thus alleviate sintering of core particles during catalytic reactions at high temperatures [2, 3].

Metal-silica core-shell material are among the most widely studied core-shell nanostructures [1, 2, 4]. The silica shell of these materials may serve as a porous membrane for preferential diffusion of different molecules, and thus can be expected to achieve different gas compositions between the internal volume inside the porous particle and the external gas stream.

In the present project, we investigate the possibility of conducting a preferential oxidation of H_2 versus CH_4 over porous nickel-silica core-shell materials. We evaluate the impact of core-shell nanostructures on catalytic selectivity from two aspects: one is the impact of nanostructure on diffusion and the other is the impact of silica shell thickness on diffusion. It is conceivable that core-shell nanostructures with different configuration would result in different kinetics in H_2 and CH_4 oxidation, and the capability of separating molecules with different sizes through porous media becomes stronger as the distance of diffusion for their molecules becomes longer.

Two core-shell materials with different configuration—namely non-hollow Ni@SiO_2 (denoted as nhNi@SiO_2) where Ni nanoclusters are evenly dispersed in a porous silica

nanoparticle, and hollow Ni@SiO_2 (denoted as hNi@SiO_2) where Ni nanoclusters decorate the inside wall of a pronounced cavity enclosed by a porous silica shell—are compared to a conventional Ni-SiO_2 catalyst (where nickel nanoclusters are dispersed on external silica surface) to investigate the impact of nanostructure on diffusion. The illustrations of these three materials are shown in the top row of Figure 1. For Ni-SiO_2, no intra-particle diffusion is required for reaction and it hence can serve as a reference.

Figure 1. Illustrations of nickel-based core silica shell materials with different configuration

To investigate whether there is a preferential diffusion of H_2 versus CH_4 over metal-silica core-shell material, first we need to study the diffusion mechanism in microporous silica nanoparticles.

Diffusion of molecules through porous media can proceed in various ways depending on the nature of the interaction between the diffusing gas molecules and the pores. When the mean free path of the diffusing gas molecules is larger than the pore size, Knudsen diffusion occurs [7]. In this regime, the gas molecules pass through the pores undergoing random collisions with the pore walls.

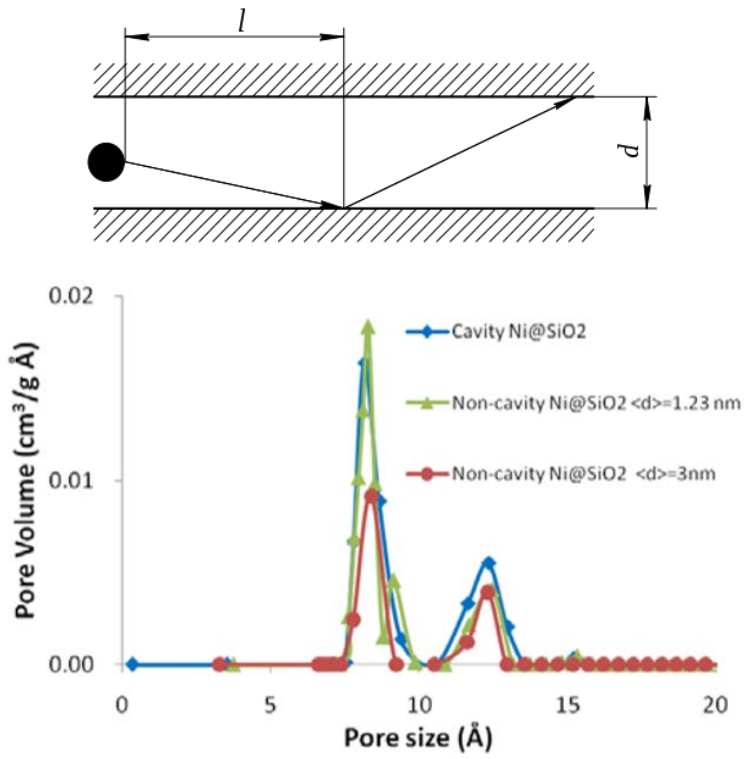

Figure 2. (top) Schematics of a molecule in a cylindrical pore in the case of Knudsen diffusion; are indicated the pore diameter (*d*) and the free path of the particle (*l*); (bottom) Pore size distribution of microporous range in both cavity and non-cavity Ni@SiO_2 structure [7]

The silica pore size of nickel–silica core-shell materials is ~0.8-1.2 nm in diameter as shown in Figure 2(b). The mean free path of hydrogen and methane are 110.6 nm and 48.1 nm respectively [21]. Therefore, the type of diffusion in the silica shell is Knudsen diffusion. The Knudsen diffusion coefficient (in cm^2/s) can be calculated as:

$$D = 97 r_p \sqrt{\frac{T}{M}} \propto \sqrt{\frac{1}{M}},$$

Where D is in m^2/s, T is in K, M is the molecular weight of the respective diffusing species, and r_p is the pore radius. Based on Knudsen diffusion, the diffusion rate is hence inversely proportional to $\sqrt{M}$. Therefore, due to the difference in molecular mass, hydrogen is expected to diffuse about 2.8-times faster than methane.

While this equation of Knudsen diffusion may be appropriate for flow in well-defined (straight and uniform) capillaries, it is not entirely precise for porous media applications in which the diffusion would be much more complicated and other elements need to be taken into consideration such as the molecular size and shape. The molecular diameters of H_2 and CH_4 are 0.289 nm and 0.371 nm respectively [6]. The kinetic diameter of H_2 and CH_4 are 0.335 nm and 0.394 nm respectively, which is estimated from the properties of the fluid at the critical point [29]. Furthermore, H_2 molecules are linear, and one can hence expect that larger methane molecules with tetrahedral structures will diffuse even more slowly into the silica pores.

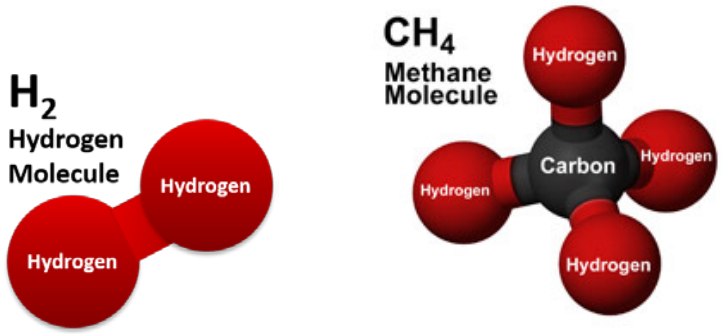

Figure 3. Illustrations of hydrogen molecule and methane molecule

The application of porous core-shell structures to preferential conversion in catalysis is not entirely new in the present work. For example, Hori et al. [5] reported a preferential oxidation of methane over *iso*-butane on silica-coated Pt. As they claimed, the difference in the relative conversion of methane to *iso*-butane should depend on the distance of diffusion for their molecules, i.e. the thickness of silica layers. Based on Fick's law ($J = -D\frac{\partial \phi}{\partial x}$, where J is the diffusion flux, D is the diffusion coefficient, ϕ is the concentration in dimensions, and x is the position), it can be derived that the capability of separating molecules with different sizes

through porous media becomes lower as the distance of diffusion for their molecules becomes shorter.

In view of the diffusion mechanism and previous findings, we expect to see a selective diffusion of hydrogen to methane over porous nickel-silica core-shell materials. However, the comparatively small difference in molecular weight, size, and shape of the molecules suggests that this is a challenging problem which requires careful tailoring of the core-shell structures.

1.1 MATERIAL SYNTHESIS

1.1.1 Synthesis of non-hollow Core-Shell Materials

In general, there are two synthesis methods for metal-silica core-shell materials: Either via coating pre-synthesized nanoparticles called “two-step synthesis” [9-11], or via a microemulsion mediated synthesis approach [5, 12, 13] also known as coating of in-situ synthesized nanocrystals or “one-step synthesis”. From the names of these two synthesis methods, we can see the main difference between “two-step synthesis” and “one-step synthesis” is when and how to coat the synthesized nanoparticles. The critical step in the two-step synthesis is to transfer pre-synthesized colloids from aqueous solution to organic solvent environment where a Stöber or a modified Stöber process is performed. For example, PVP which is an amphiphilic polymer is able to stabilize colloidal particles in water. PVP coated particles can then be transferred into a mixture of water-ammonia-ethanol and be directly coated with silica shells via tetraethyl orthosilicate (TEOS) hydrolysis and condensation.

Microemulsions are isotropic, macroscopically homogeneous, and thermodynamically stable solutions containing at least three components: a polar phase (usually water), a nonpolar phase (usually oil) and a surfactant, frequently in combination with a cosurfactant [17]. In microemulsion methods, metal nanoparticles are formed in the microemulsion and then hydrolysis and polycondensation of tetraethylorthosilicate (TEOS) is performed in the microemulsion. By this preparation method, nanoparticles of various metals or metal oxides (such as Fe_3O_4, Ni, Co, Pt, Rh, etc) can be covered uniformly with silica layers. There are two types of microemulsion including normal (oil droplets dispersed in water) and reverse (water droplets dispersed in oil) both inorganic salts and organometallic precursors. Water is not only used to stabilize micelles, but also serves as a reactant for TEOS hydrolysis. Silica nucleation is better controlled in the "one-step synthesis" compared to "two-step synthesis", since silica nucleation and growth occur within the boundaries of the nanometer-sized droplets. We hence utilize this approach for the synthesis of the core-shell materials in the present work.

1.1.2 Synthesis of Core-Shell Materials with Hollow Structure

In addition to the traditional dense core-shell materials, core-shell materials with hollow structures also have drawn considerable attention in recent years. The advantage of a hollow core-shell nanostructure is that more surface area of active components is exposed to reactants, which is desirable as a heterogeneous catalyst. Hollow core-shell materials are typically prepared by selective etching the core particles [10] or the shells [14]. In contrast to that approach, Whaley [8] found that the existence of nickel hydrazine complexes stabilizes the micelles inside a reverse microemulsion during the TEOS hydrolysis, resulting in the formation of hollow structure in $Ni@SiO_2$. Unlike most other routes to create cavity structures in a core-shell

material, which involve complex, multi-step syntheses with sacrificial material layers, this synthesis constitutes a one-pot approach without sacrificial materials.

2.0 EXPERIMENTAL SECTION

2.1 MATERIAL SYNTHESIS

All materials were synthesized using procedures that were previously established in our research group. Standard synthesis procedures include solution synthesis, surfactant removal by calcinations, external nickel removal by etching, and finally surface cleaning for materials used for reactive testing [8].

2.1.1 Solution synthesis

Nickel-silica core-shell material is synthesized in a reverse microemulsion mediated sol-gel process [8]. For hollow Ni@SiO_2 (denoted as hNi@SiO_2), a mixture of 10g Brij58 (≥99%, Sigma-Aldrich) and 50 mL cyclohexane (≥99%, Sigma-Aldrich) in a three-neck flask was heated up to 50^{o}C in oil bath under stirring (with stirring rate 340 rpm). The nickel nitrate aqueous solution (1.5 mL, 1.0 M salt solution) was added dropwise. After ~30 minutes stirring, hydrazine hydrate (1.5mL, Sigma-Aldrich) was added dropwise and the mixture was stirred for another hour. Next, ammonium hydroxide solution (3 mL, 28 wt.%, Sigma-Aldrich) was added dropwise to the previous solution. After 1 hour stirring, 5g tetraethoxysilane (TEOS, ≥99%, Sigma-Aldrich) was added dropwise to the previous soluition. Hydrolysis and condensation of the silica precursors were allowed to proceed for 2 hours at 50°C. Then hNi@SiO_2 was precipitated by

adding 2-propanol and washed three times by centrifugation and redispersion in 2-propanol. As for Ni@SiO_2 without cavity structure, the synthesis procedure is easily adjusted from the recipe for hNi@SiO_2 but the addition of hydrazine hydrate is omitted.

2.1.2 Surfactant removal

This step is applicable for hNi@SiO_2 and nhNi@SiO_2. After drying in the hood, Ni@SiO_2 samples were calcined at 500^{o}C for 2 hours under 0.5 SLM air stream in a Thermolyne 79300 tube furnace. The color of the calcined sample is grey indicating the formation of NiO (in contrast, metallic Ni results in a black color).

2.1.3 Etching process and surface purification

After previous treatment, the material is etched with HNO_3 (70%, Sigma-Aldrich) to remove any extraneous nickel outside the silica shell. In this step, 0.2g of the material was dispersed in 20mL HNO_3 and 20mL DI water for 30 minutes (with a stirring rate 240rpm). Next, the etched material is washed with DI water, centrifuged, and redispersed three times. Then the sample is placed in the hood for drying. Another calcination cycle is performed to remove any residual acid and impurities. The sample is calcined in air (0.5 SLM) at 500^{o}C for 2 hour with a heating rate of 5°C/min.

As comparison materials, Ni-SiO_2 is also synthesized by a simple deposition-precipitation method. The synthesis procedure can be found in Section 1.01(a)(i)Appendix B.

2.2 MATERIAL CHARACTERIZATION

2.2.1 Transmission Electron Microscopy (TEM)

Catalyst morphology is determined by both transmission electron microscopy (TEM) and a high resolution transmission electron microscopy (HRTEM). In the TEM sample preparation, a tiny amount of the material is grinded in the mortar and dispersed in ethanol. The solution is sonicated about 5 minute for better dispersion. After that, two to three drops of the solution are dispersed on a TEM grid and then dried.

2.2.1.1 TEM images of nhNi@SiO_2

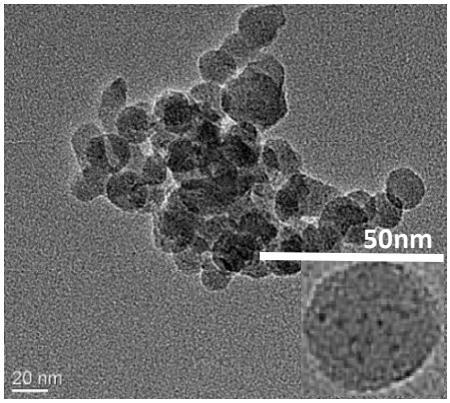

Figure 4. TEM images of nhNi@SiO_2

Figure 4 shows a typical TEM image of nhNi@SiO_2 sample. The diameter of the spherical particle is ~30nm. The nickel particles are evenly embedded inside the silica shell. There is hence no well-defined, uniform silica shell thickness; some nickel particles are located

near the silica shell surface while others are embedded deeply into the silica particle. The material is a grey powdered sample. The nickel loading is 5.3wt%.

2.2.1.2 TEM images of hNi@SiO_2

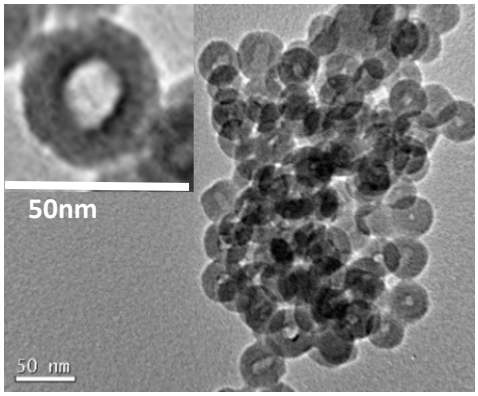

Figure 5. TEM images of hNi@SiO_2

The diameter of the spherical particle is ~30nm, i.e. virtually identical to the non-hollow nhNi@SiO_2 particles. However, there is a pronounced cavity structure inside the silica shell, which is ~10nm in diameter on average. The grey ring is the porous silica shell with a thickness ~10nm. The inner wall of silica shell is decorated with a dark ring of small nickel clusters (~1-2nm). The material is a grey powdered sample. The nickel loading is 4.6wt%.

2.2.1.3 TEM images of Ni-SiO_2

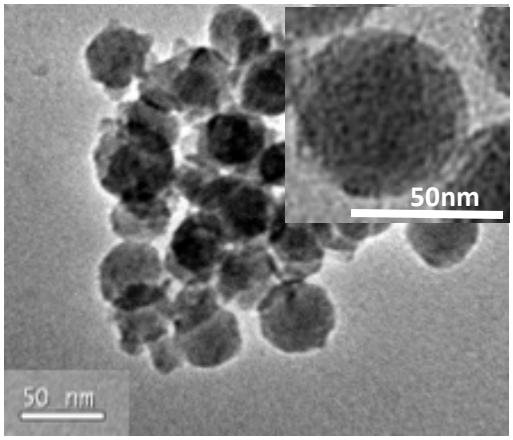

Figure 6. TEM images of Ni-SiO_2

The diameter of the spherical silica particles prepared for these materials is ~45nm. The nickel particles are randomly deposited on the external surface of silica shell. There are no nickel particles inside the silica shell. The material is a grey powdered sample. The nickel loading is 4.0wt%.

2.3 REACTIVITY TESTS SETUP

The reactive tests are conducted in fixed bed. Powdered catalytic materials are inserted into a 5 mm ID quartz glass tube. Both end of the materials are supported by quartz wool. The tube reactor is placed within a furnace. A thermocouple is inserted into the tube reactor to monitor reaction temperature. Make sure that the tip of the thermocouple is situated within 1 mm of the end of the catalyst zone. The temperature in the reaction zone is controlled by the temperature program set on the furnace. Mass flow controllers (MKS Instruments Inc.) are used to feed reaction gases diluted with inert gas. The products are analyzed by mass spectrometer.

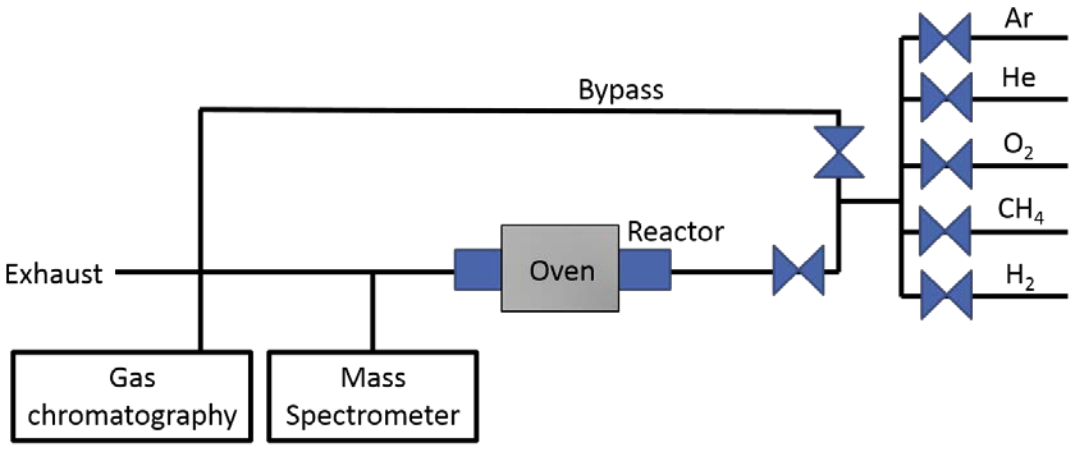

Figure 7. Flow chart of reaction setup

During the reactive test, it is observed that the CH_4 signal at 700^oC precedes the signal at room temperature when feeding CH_4 over nickel-silica core-shell materials. It is verified that the volumetric change and temperature change contribute to the preceding signal breakthrough at reaction temperature. The detailed explanation can be found in Section 1.01(a)(i)Appendix C.

3.0 RESULTS: REACTIVITY OF NICKEL- SILICA CORE-SHELL CATALYSTS IN H_2 AND CH_4 OXIDATION REACTION

3.1 OXIDATION OF UNMIXED H_2 AND CH_4 OVER NICKEL-SILICA CORE-SHELL MATERIALS

In this section, we investigate the possibility of conducting a preferential oxidation of H_2 versus CH_4 over porous nickel-silica core-shell materials, and evaluate the impact of core-shell nanostructures on diffusion. It is expect to see different kinetics of H_2 and CH_4 oxidation on nhNi@SiO_2, hNi@SiO_2 and Ni-SiO_2 due to the different pathways of these catalysts, which result from their different configurations.

200 mg of each material was inserted into a quartz glass tube with 5 mm in diameter. The nhNi@SiO_2/Ni-SiO_2/hNi@SiO_2 (with 10nm shell in thickness) was first oxidized in air flow at 500^{o}C for 30 minutes to make sure the nickel particles were fully oxidized at the start of the reactivity tests. After that, 6.25 sccm CH_4 and 6.25 sccm H_2 (diluted with inert gas) were flow over each sample at 700^{o}C respectively.

3.1.1 H_2 oxidation over nhNi@SiO_2 and hNi@SiO_2

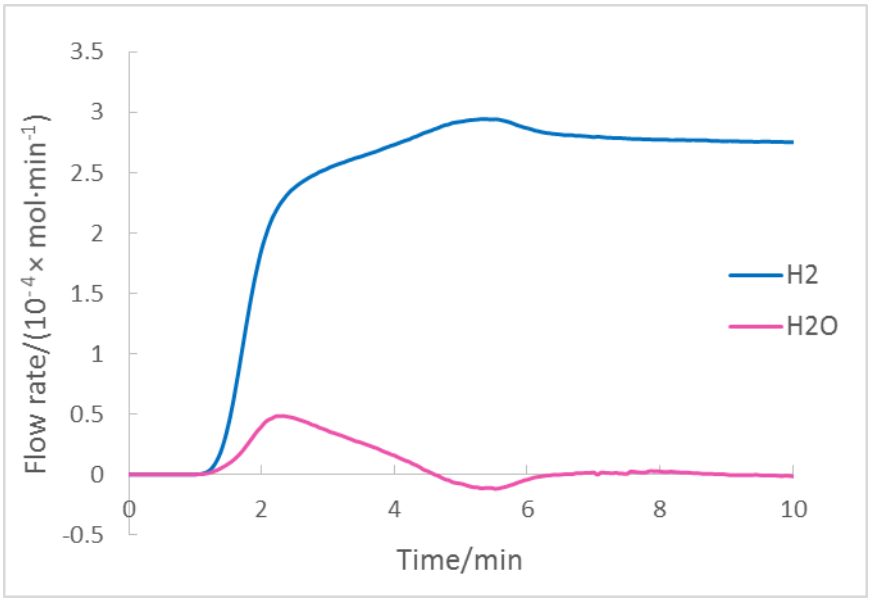

Figure 8. H_2 oxidation over nhNi@SiO_2 at 700 ºC. Catalyst weight = 0.2g (5.3wt%Ni loading), feed stream: 6.25 cm^3/min H_2 + 6.25 cm^3/min He

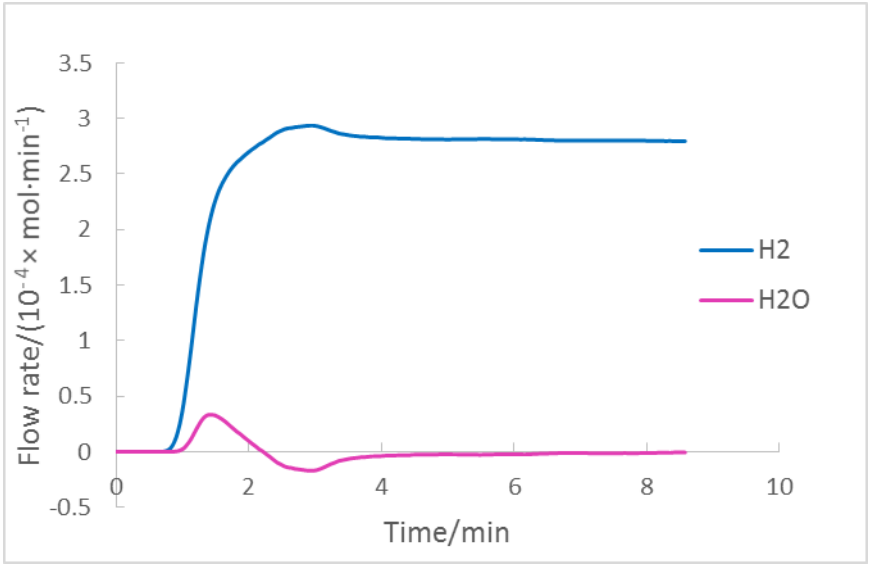

Figure 9. H_2 oxidation over hNi@SiO_2 at 700 ºC. Catalyst weight = 0.2g (4.6wt%Ni loading), feed stream: 6.25 cm^3/min H_2 + 6.25 cm^3/min He

Figures 8 and 9 show the product stream composition (as volumetric flows) versus time for H_2 feeds over nhNi@SiO_2 (fig. 8) and hNiSiO_2 (fig. 9), respectively. As expected, one can

see in both cases the formation of water as product of the rapid reaction of H_2 with the NiO cores. After a few minutes, water formation stops, indicating that the oxygen reservoir in the NiO nanoclusters has been exhausted.

Interestingly, when feeding H_2 over nhNi@SiO_2 and hNi@SiO_2, it took less time for water to generate and be flushed out of catalyst bed completely for the hollow structures (hNi@SiO_2) than for the non-hollow ones (nhNi@SiO_2). The similarity between the two catalysts in all aspects other than the location of the Ni nanoclusters allows us to correlate this difference in reactivity directly with the different nanostructure: For the core-shell materials without the central cavity, the nickel nanoclusters are randomly embedded inside the silica shell, i.e. some clusters are located near the outer surface of the silica shells while others are dispersed deeply inside. Hence, when H_2 diffuses into nhNi@SiO_2, it will react with NiO clusters near the outer silica surface first. Only once these clusters have been reduced, H_2 will (have to) further diffuse into the silica shell to react with remaining NiO clusters (see schematic in fig. 10a). In contrast to that, for hNi@SiO_2, NiO clusters are located on the inner wall of the silica shell, so that the uniform shell thickness results in a uniform diffusion pathway for H_2 to all NiO clusters (see fig. 10b). This could explain the delay in the leading edges in the water signal and the H_2 signal: silica is hydroscopic, so that water formed on a NiO cluster will adsorb on the silica on the diffusion out of the silica nanoparticle, resulting in a “chromatographic delay” in the appearance of this species in the effluent stream. For nhNi@SiO_2, this delay is negligible as initial water formation occurs on the NiO clusters closest to the external surface. However, for hNi@SiO_2 the water formation occurs uniformly inside the cavity and hence results in a diffusional delay from the onset. This difference also explain the more narrow appearance time

of the water pulse for the hNi@SiO_2 due to the well-defined and uniform location of the NiO clusters in this material.

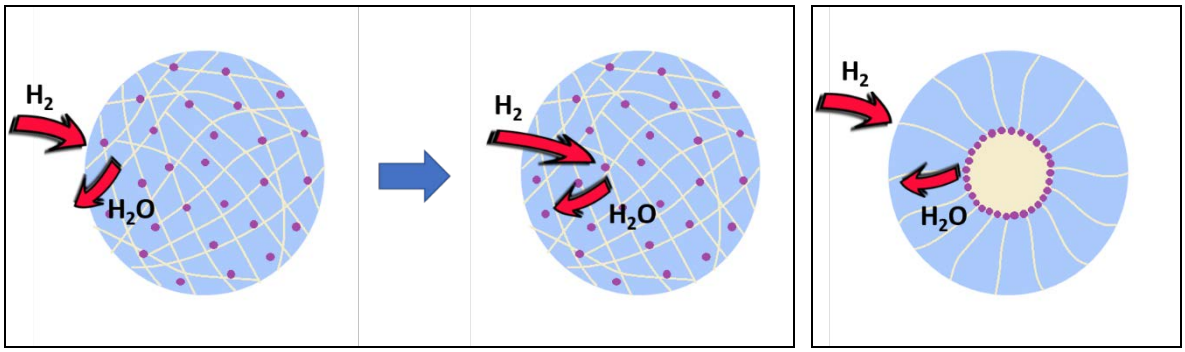

(a) (b)

Figure 10. Schematics of how H_2 diffuses into and H_2O diffuses out of (a) nhNi@SiO_2, (b) hNi@SiO_2

Another interesting phenomenon, which is common in both materials, is the small but distinct "hump" in hydrogen signal, at which the detected hydrogen flow exceeds the feed gas flow, thus indicating hydrogen formation. Again, the phenomenon can be correlated directly with the catalyst nanostructure: For nhNi@SiO_2, during H_2O diffusion out of the silica pores, H_2O is increasingly likely to encounter already reduced Ni nanoclusters and thus be reduced to H_2 in an oxidation reaction of the Ni, i.e. the reverse reaction of the H_2 oxidation with NiO (see fig.10 (left)). This also explains the very slowly trailing end of the water signal as a result of this increasingly important reverse reaction as the NiO clusters are being reduced more and more deeply inside the silica particle and hence the importance of the reverse reaction increases with time.

For hNi@SiO_2, the generated H_2O has conceptually two "different" routes to diffuse out of the silica particle, as shown in Figure 10 (right): one is "direct" diffusion out though the silica pores, while the other involves diffusing through the silica pores only after entering the central cavity structure. Unlike for nhNi@SiO_2, only the second route results in the possibility of H_2O reduction to H_2, as the first route would not result in any contact between H_2O and Ni. That can

explain the much smaller width of the “hump” in hydrogen signal and the much reduced trailing edge of the water signal.

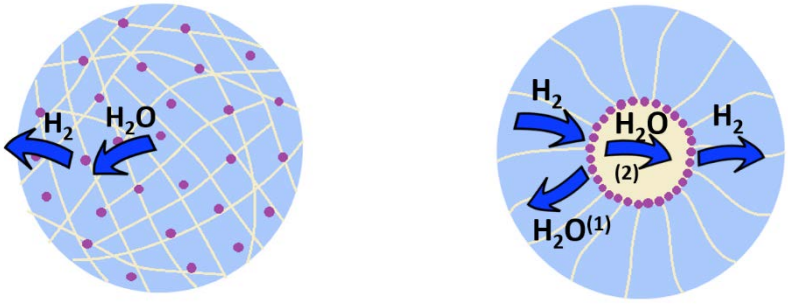

Figure 11. Illustrations of hydrogen formation by H_2O reduction in nhNi@SiO_2 (left) and hNi@SiO_2 (right)

It is noticed that in both cases, the hump in the H_2 signal coexists with a negative water flow (calculated from a hydrogen balance in the system), in agreement with the explanation of the additional H_2 as a result of water consumption.

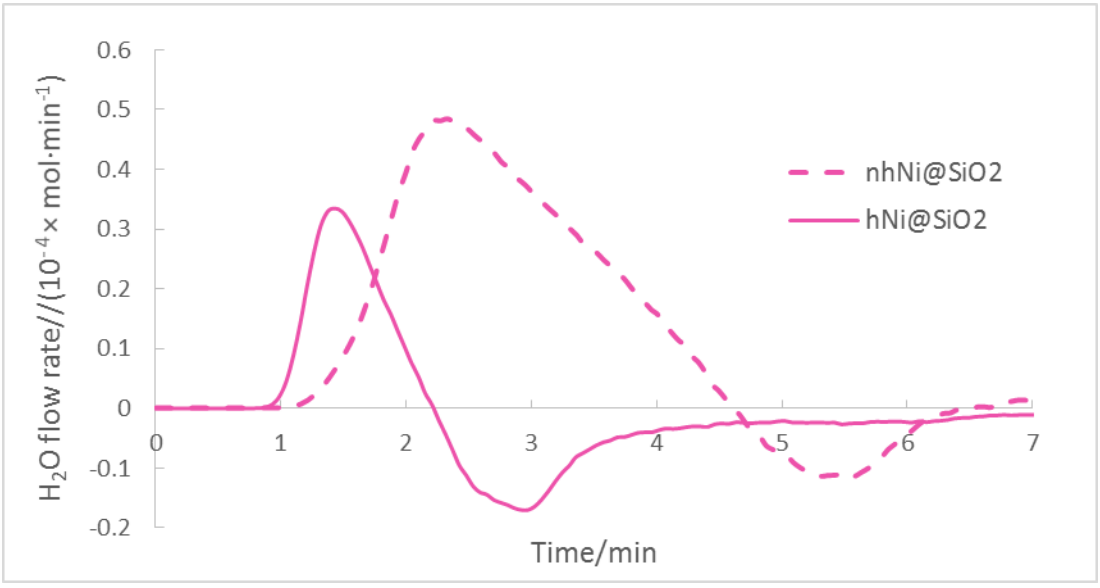

Figure 12. H_2O flow rate versus time on nhNi@SiO_2 and hNi@SiO_2

Figure 12 indicates that there is less availability of reducible oxygen sites in hollow materials. Based on EDX results (which is used to determine the elemental composition of materials), the Ni loadings in hollow and non-hollow materials are 4.6wt% and 5.3wt%, respectively. The integral H_2 conversions in both cases are 0.8 (nhNi@SiO_2) and 0.72 (hNi@SiO_2) respectively (see section 3.1.3), which is agreement with the phenomenon observed.

3.1.2 CH_4 oxidation over nhNi@SiO_2 and hNi@SiO_2

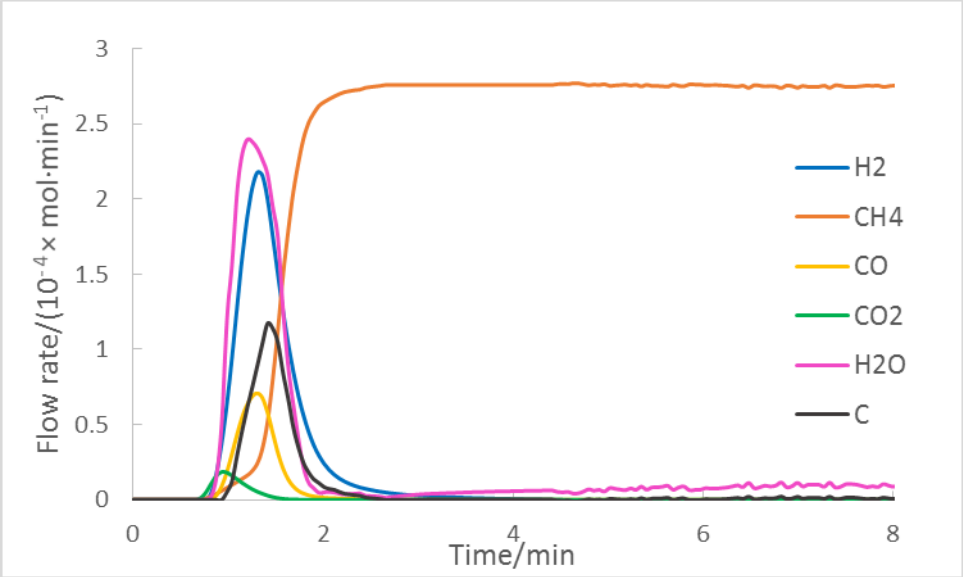

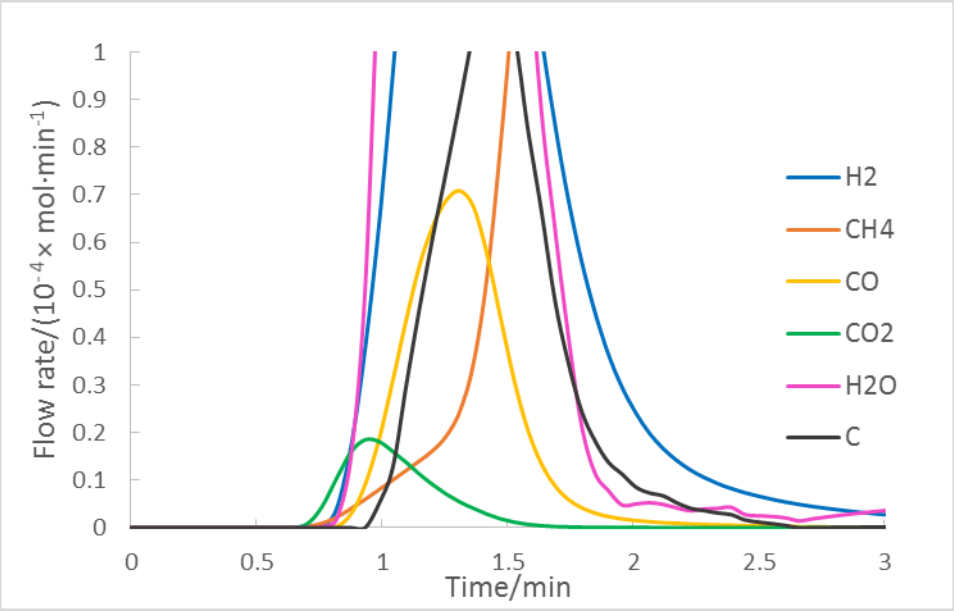

Figure 13**. CH_4 oxidation over nhNi@SiO_2 at 700ºC. Catalyst weight = 0.2g (5.3wt% Ni loading), feed stream: 6.25cm^3/min CH_4 + 6.25 cm^3/min He. The bottom graph is the enlarged view that allows to see the occurrence of the minor reaction products.**

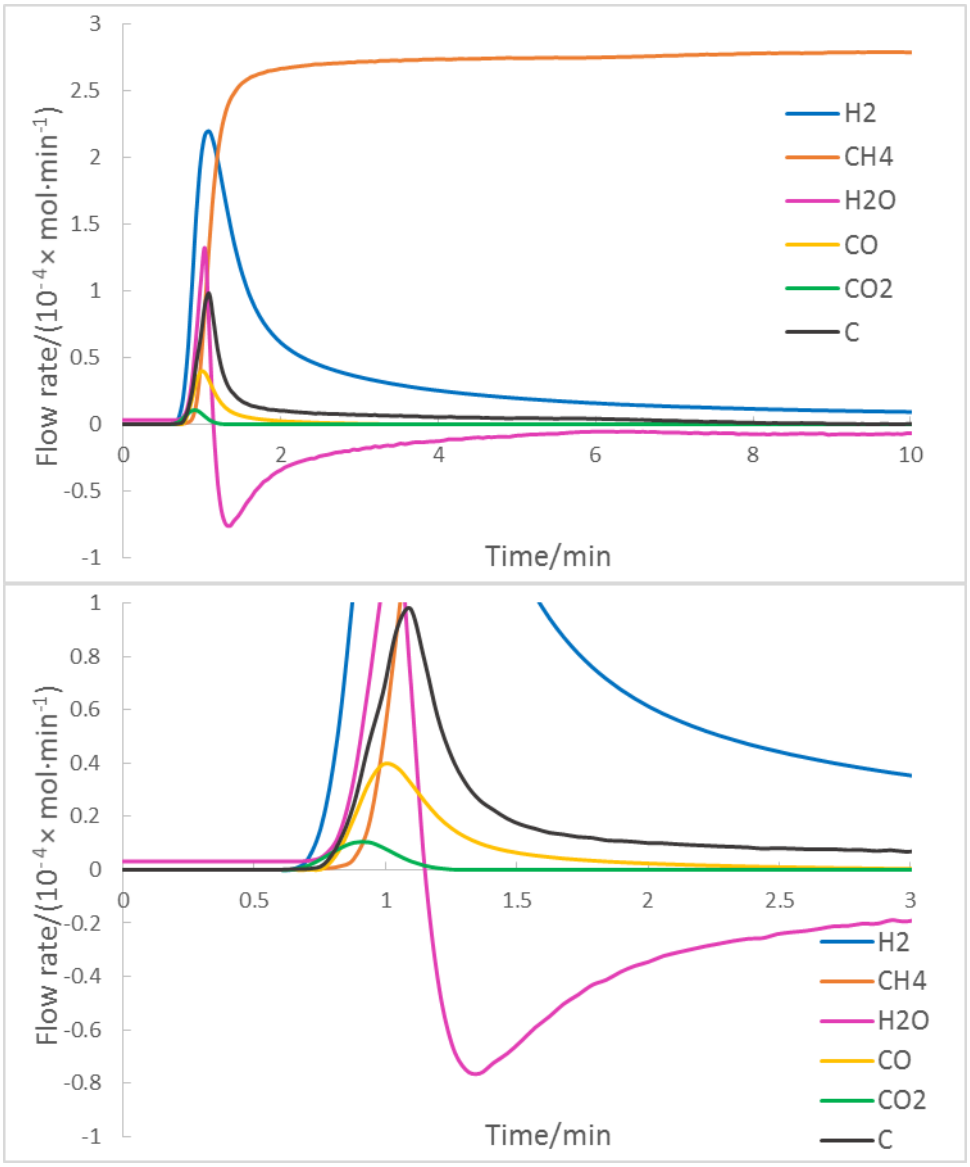

Figure 14. CH_4 oxidation over hNi@SiO_2 at 700ºC. Catalyst weight = 0.2g (4.6wt% Ni loading), feed stream: 6.25cm^3/min CH_4 + 6.25 cm^3/min He. The bottom graph is the enlarged view that allows to see the occurrence of the minor reaction products.

When feeding CH_4 over nhNi@SiO_2 and hNi@SiO_2, there are several possible reactions that can occur in both nanostructures:

$CH_4 + 4NiO \rightarrow CO_2 + 2H_2O + 4Ni$, methane total oxidation;

$CH_4 + NiO \rightarrow CO + 2H_2 + Ni$, methane partial oxidation;

$CH_4 \rightarrow C + 2H_2$, methane cracking.

Figures 13 and 14 show the product stream composition (as volumetric flows) versus time for CH_4 feeds over nhNi@SiO_2 (fig. 13) and hNi@SiO_2 (fig. 14), respectively. As expected, one can see in both cases the formation of H_2, CO, CO_2 and water as product of the rapid reaction of CH_4 with the NiO cores. After a few minutes, product formation stops, indicating that the oxygen reservoir in the NiO nanoclusters has been exhausted. Based on Knudsen diffusion, the gas diffusion order in this system should be: H_2>CH_4>H_2O>CO>CO_2, however, the experimental results show the order of appearance for the components in the effluent stream as: H_2>CH_4 >H_2O>CO_2>CO. Clearly, the temporal product spectrum is a result of both diffusion and reaction events: At the start of the NiO reduction, there are the most oxygen sites available and thus methane total oxidation is more likely to happen. So one can observe that CO_2 shows earlier than CO signal.

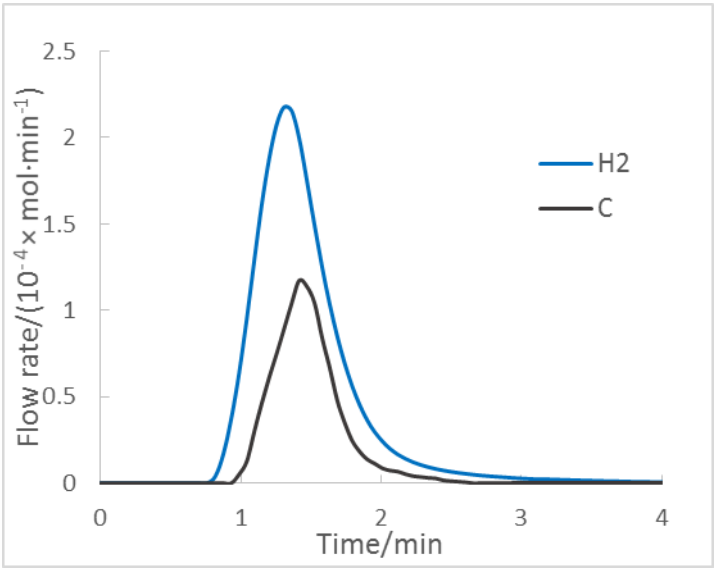

Figure 15. H_2 and carbon molar flow rate versus time on nhNi@SiO_2

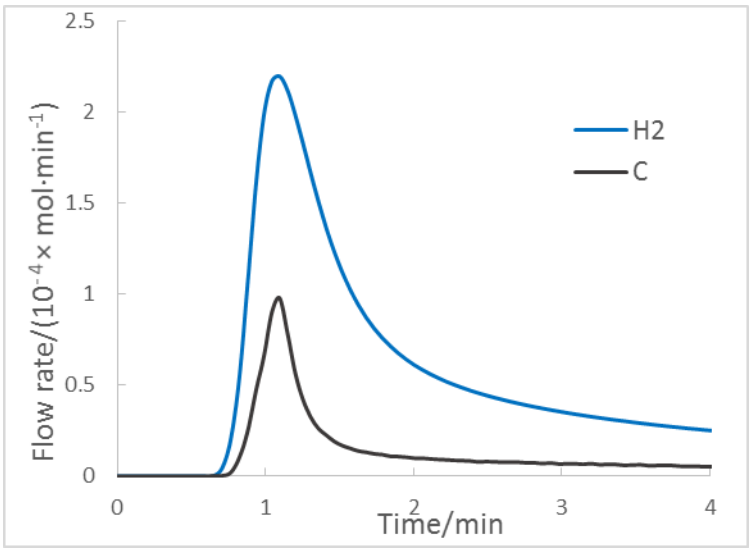

Figure 16. H_2 and carbon molar flow rate versus time on hNi@SiO_2

Comparing the hydrogen flow rates in both experiments (fig. 15, 16), we observe that the shape of these two signals are quite different: H_2 signal over nhNi@SiO_2 has symmetric shape while the H_2 signal over hNi@SiO_2 shows a much slower decline over time. Note that this is opposite to the trends seen in the H_2 oxidation experiment before, where the non-hollow structure showed the much longer trailing end (i.e. higher asymmetry) than the hollow structure. It is hence unlikely that secondary reactions of steam with the Ni clusters cause this phenomenon. Instead, the explanation can be found in a different hydrogen production channel (not present in the H_2 oxidation system): Nickel is known to be an excellent methane cracking catalyst [22, 32], and the occurrence of the very long trailing end of the hydrogen production curve long past the point where oxidative products occur suggests that it is methane cracking that results in continued hydrogen production. This seems reasonable because the cavity structures in hNi@SiO_2 allow sufficient space for carbonaceous deposits to grow, while the small pore size in the non-hollow structure results in a rapid and sudden completion of the reaction after complete

consumption of the available oxygen in the NiO clusters, as reflected in the non-monotomic, abrupt end of methane consumption and hydrogen production at t~ 4 min.

A closer look at the carbon oxidation products (see fig. 17) shows that CH_4 partial oxidation is dominant over total oxidation for both catalysts, but more CO formation occurs on nhNi@SiO_2. The less CO formation correlates to the shutdown of oxidation reaction in hollow material, which is discussed in the next section. However, the CO formation shows a much longer trailing end on hNi@SiO_2, and correspondingly we observe a negative water formation from ~1.2 min, suggesting a CO formation via steam reforming of methane. However, this hypothesis contradicts to the fact that CH_4 conversion drops dramatically to a very low value at ~ 2 min. As we discussed previously, there is more coke formed in hollow material, so the stronger CO formation on hollow material after ~1.5 min could be explained by the reaction between carbonaceous deposits and steam.

Another interesting point is more CO_2 formation occurring on nhNi@SiO_2 than for hNi@SiO_2. This can again be explained by the different nanostructure between the two catalysts: For nhNi@SiO_2, there are two pathways to generate CO_2: either by methane total oxidation (direct formation) or by CO oxidation (indirect formation). When methane diffuses into nhNi@SiO_2, it will encounter nickel oxide particles and form either CO or CO_2, likely depending on the degree of oxidation of the Ni cluster. Upon diffusion out of the catalyst particle, any CO formed in this primary oxidation step is very likely to hit another nickel oxide particle to form CO_2. In contrast to that, for hNi@SiO_2, nickel oxide particles are uniformly located on the inner wall of the silica shell so that CO and CO_2 can diffuse out through pores directly after reaction. Hence, the difference in CO product profiles could be explained in an analogous way to the water profiles in the H_2 oxidation experiments.

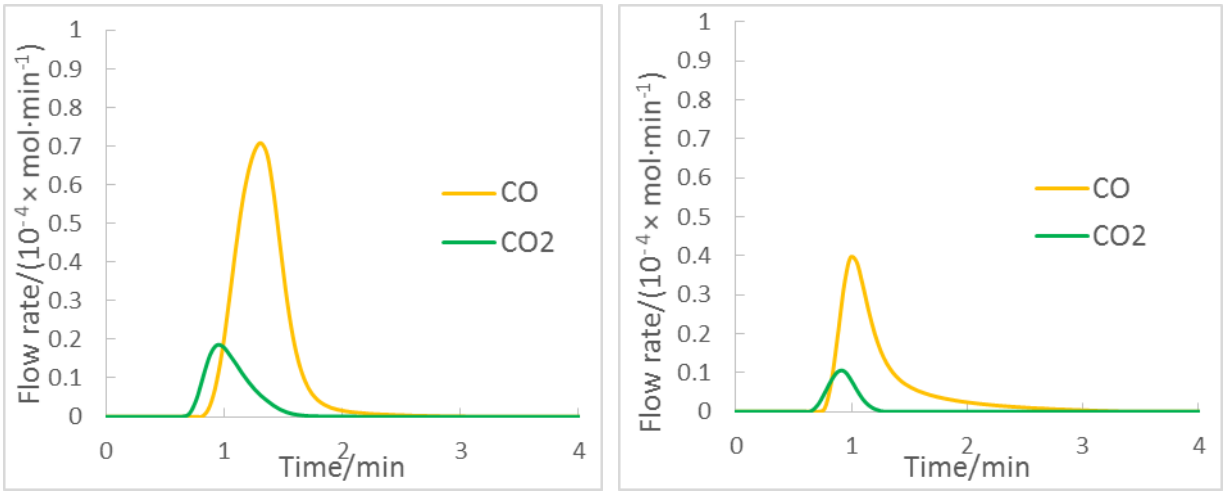

Figure 17. Production rates of CO and CO_2 over (a) nhNi@SiO_2, (b) hNi@SiO_2

3.1.3 H_2 and CH_4 conversions over nhNi@SiO_2 and hNi@SiO_2

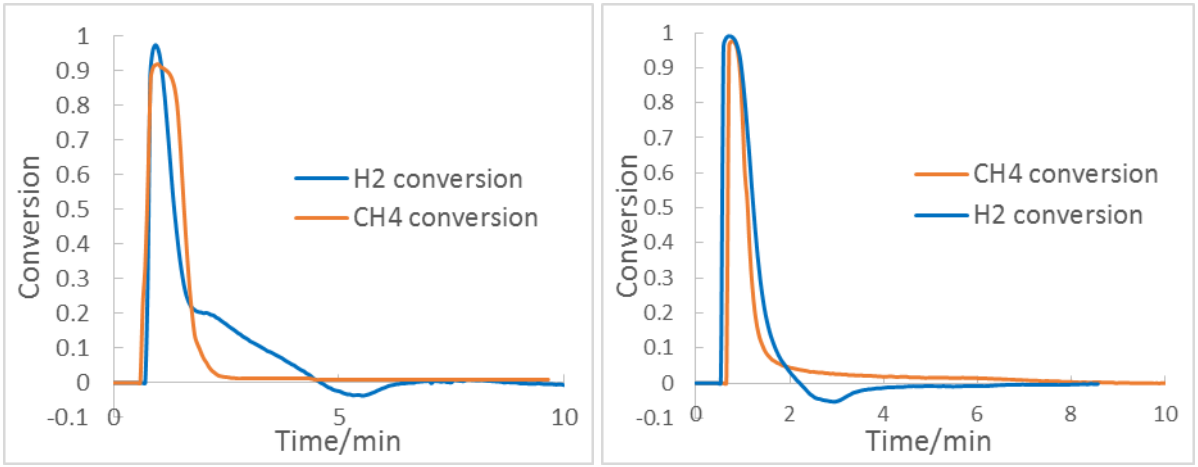

Figure 18. Conversion of H_2 and CH_4 over (a) nhNi@SiO_2, (b) hNi@SiO_2

Table 1. Integral H_2 and CH_4 conversion on nhNi@SiO_2 and hNi@SiO_2

	H_2 conversion	CH_4 conversion
nhNi@SiO_2	0.80	0.83
hNi@SiO_2	0.72	0.59

Figure 18 shows the conversions of H_2 and CH_4 over nhNi@SiO_2 (fig. 18a) and hNi@SiO_2 (fig. 18b) calculated from the effluent stream data in the previous section. One can see that only for hollow material, the H_2 conversion precedes the CH_4 conversion, suggesting that H_2 diffuses more easily than CH_4 in the silica pores and a shell with uniform thickness can enhance the selectivity. An alternate conclusion would be a different reactivity of H_2 vs CH_4 (which is generally less reactive in oxidation reactions than hydrogen) with NiO. However, we can calculate from the leading edge of the conversion plots an initial conversion rate of 8.4 min^{-1} for H_2 and 7.5 min^{-1} for CH_4, i.e. sufficiently close agreement to exclude different reactivities as the reason for the delay. The negative values of H_2 conversion correspond to the H_2 formation by H_2O reduction during H_2O diffusing out. It is hence expected that the effect of "selective" diffusion of reactants could be enhanced with the increase of shell thickness.

The H_2 conversion curve on nhNi@SiO_2 shows a gentle-slope decline after reaching the maximum conversion. During this period, the formed H_2O are under the process of diffusing out, which tends to encounter an already reduced nickel particle to conduct the reverse reaction of H_2 oxidation. Simultaneously H_2 oxidation reaction is still going on. As a result, a combination of H_2 oxidation and reverse reaction of H_2 oxidation reflects a slower slope in H_2 conversion curve on nhNi@SiO_2. This is not observed in hNi@SiO_2 because the higher pressure in cavity due to water formation tends to force water diffusion out of silica shell more quickly.

For nhNi@SiO_2 catalyst, CH_4 conversion starts later and ends later. While in the hNi@SiO_2 test, CH_4 conversion starts after H_2, ends before H_2 and shows a much longer trailing end. Correspondingly, the integral CH_4 conversion on hNi@SiO_2 is much lower than that on nhNi@SiO_2, suggesting that the oxidation reactions on hollow material shuts down at some point and then coking keeps going on. It is likely that in hollow structure Ni nanoclusters agglomerate

at reaction temperature and carbonaceous deposits grow and wrap the agglomerated Ni nanoclusters inside the cavity that block the contact between reactant gases and active sites. TEM images of hNi@SiO_2 after reduction in H_2 feed at 700^oC for 20 minutes (fig. 20) confirm that Ni nanoclusters agglomerate during the reaction at 700^oC. The lower H_2 conversion on hNi@SiO_2 test correlates to a slightly lower Ni loading in hollow material.

3.1.4 Coking resistance of hollow Ni@SiO_2

Nickel is known to be an excellent methane cracking catalyst [22, 23], and as a result, coking becomes an inevitable and well-documented issue in CH_4 oxidation reaction over Ni-based catalysts. The differences in the nanostructure of hNi@SiO_2, versus nhNi@SiO_2 result in strongly different coking behavior, as seen and discussed in the results of above reactivity tests. In particular, the cavity structure of hNi@SiO_2 offers ample space for carbonaceous deposits. Therefore, it is of a great importance to learn how the materials look like after reaction so that we can further verity our statement about the different coking behavior in nhNi@SiO_2 and hNi@SiO_2.

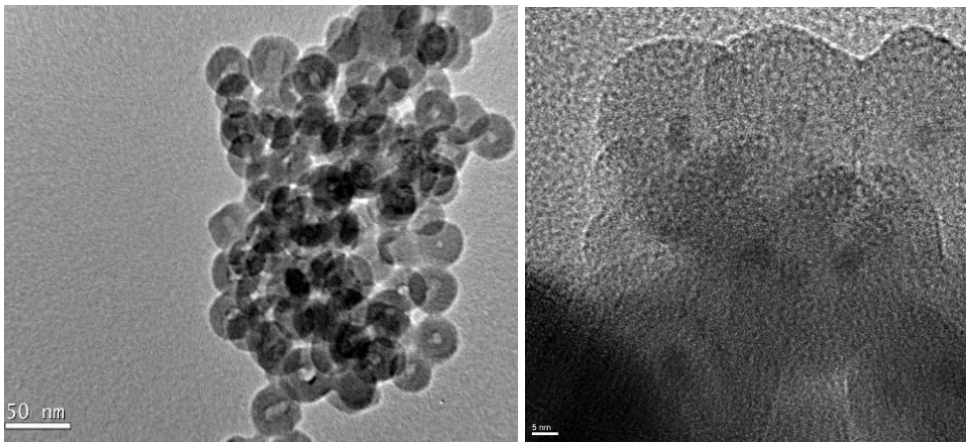

Figure 19. (a) TEM of hNi@SiO_2 before reaction; (b) TEM images of hNi@SiO_2 after reduction in CH_4 at 700^oC for 20 minutes (the scale bar is 5 nm)

To investigate coking resistance of $Ni@SiO_2$ with cavity structure, the material after reduction in CH_4 flow at 700°C for 20 minutes was investigated in TEM. As shown in figure 19(b), after reaction with CH_4 at 700°C, the nickel nanoclusters appear to agglomerate and it seems that the cavity structures no longer exist, i.e. that the hollow silica structure did not survive the demanding reaction conditions and collapsed. However, TEM does not allow for easy distinction between carbon and nickel inside the silica cavity. As we discussed previously in section 3.1.2, the cavity in $hNi@SiO_2$ allow sufficient space for carbon formation. It is hence speculated that the dark area inside the silica shell shown in TEM images is likely to be nickel and carbon. Since H_2 oxidation over $Ni@SiO_2$ will not introduce carbonaceous deposits, learning the material structure after reduction in H_2 may help us to understand if carbon fills the cavity.

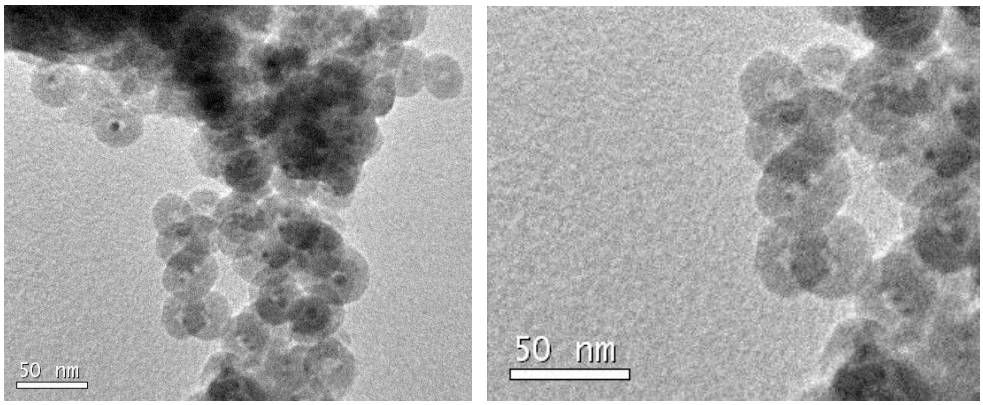

Figure 20. TEM images of $hNi@SiO_2$ after reduction in H_2 at 700°C for 20 minutes

According to the TEM images (fig. 20) of $hNi@SiO_2$ after reduction in H_2 at 700°C for 20 minutes, the nickel clusters did agglomerate at reaction condition while the cavity structure still exists, which confirms our speculation that the darker areas in the TEM images of $hNi@SiO_2$ after reduction in CH_4 are Ni nanoclusters and carbonaceous deposits. In other words, the cavity structure won't collapse after reaction, and the disappearance of hollow structure in

hNi@SiO_2 after reduction in CH_4 is caused by the formation of carbon which grow and fill in the cavity structure.

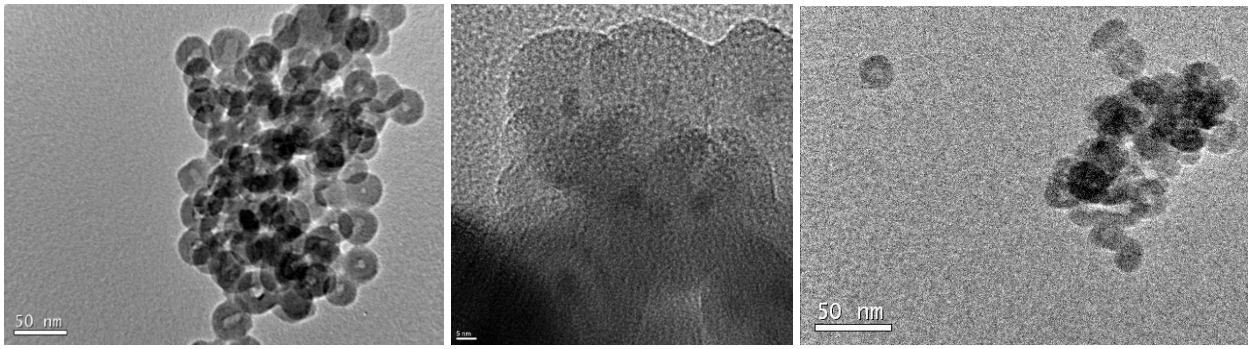

(a) (b) (c)

Figure 21. TEM images of hNi@SiO_2 (a) before thermal treatment; (b) after reaction in CH4 at 700ºC for 20 minutes; (c) after being re-oxidized in air at 700ºC for 30 minutes.

To further demonstrate that the cavity structure does not collapse after reaction in CH_4 flow, the materials which had been treated in CH_4 flow at 700^{o}C for 20 minutes were re-oxidized in air at 700^{o}C for a period of time to burn off the carbon. TEM images (fig. 21(c)) again verify that the cavity structure still exist after thermal treatment.

3.1.5 H_2 oxidation and CH_4 oxidation over Ni-SiO_2

To investigate how porous silica shell influences gas diffusion, as a comparison, the same experiments of H_2 oxidation and CH_4 oxidation were conducted on Ni-SiO_2 which doesn't have diffusion problem because nickel particles are deposited on spherical silica surface.

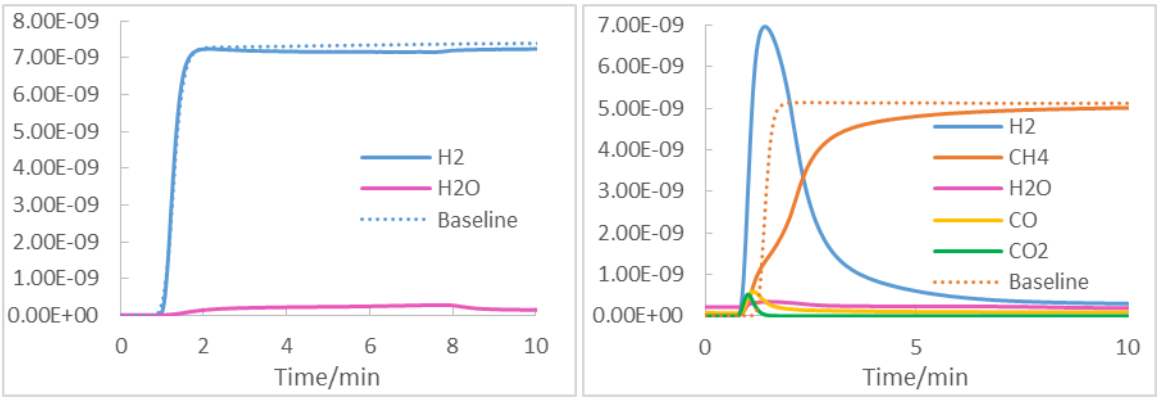

Figure 22. H_2 and CH_4 oxidation over Ni-SiO_2 at 700°C, catalyst weight = 0.2g (4wt% Ni loading), feed stream: 6.25 cm^3/min H_2/CH_4 + 6.25 cm^3/min He.

Figures 22 shows the product stream composition versus time for H_2 and CH_4 feeds over Ni-SiO_2. We see the weak formation of H_2O in H_2 feed, and weak formation of CO, CO_2 and water as product of the rapid reaction of CH_4 with the NiO cores. But a strong H_2 formation is observed at the same time. The results indicate Ni-SiO_2 seems to have less reactive sites. TEM sample of Ni-SiO_2 after reaction in CH_4 at 700°C were made to investigate the reason for the low reactivity on Ni-SiO_2. As seen in Figure 23, severe sintering of nickel nanoparticles on the silica surface occurred at the high reaction temperature. The larger Ni NP size not only reduces the reaction rate due to the smaller exposed surface area, but furthermore results in a strong limitation in the reaction as larger NiO NPs also impose a much longer diffusion path for the oxygen from the core of the NiO nanoparticle to the surface of the particle. Our results suggest that for NiO nanoparticles larger than a critical size, the oxygen reservoir inside the particle is effectively unaccessible at these reaction conditions (i.e. the diffusion rate becomes sufficiently slow that the diffusion limitations effectively shut down further reaction). Solunke, in our group, has previously reported a similar phenomenon for Fe-based oxygen carriers in chemical looping hydrogen generation [24]. Compared with Ni-SiO_2, hNi@SiO_2 and nhNi@SiO_2 show more stability under reaction conditions.

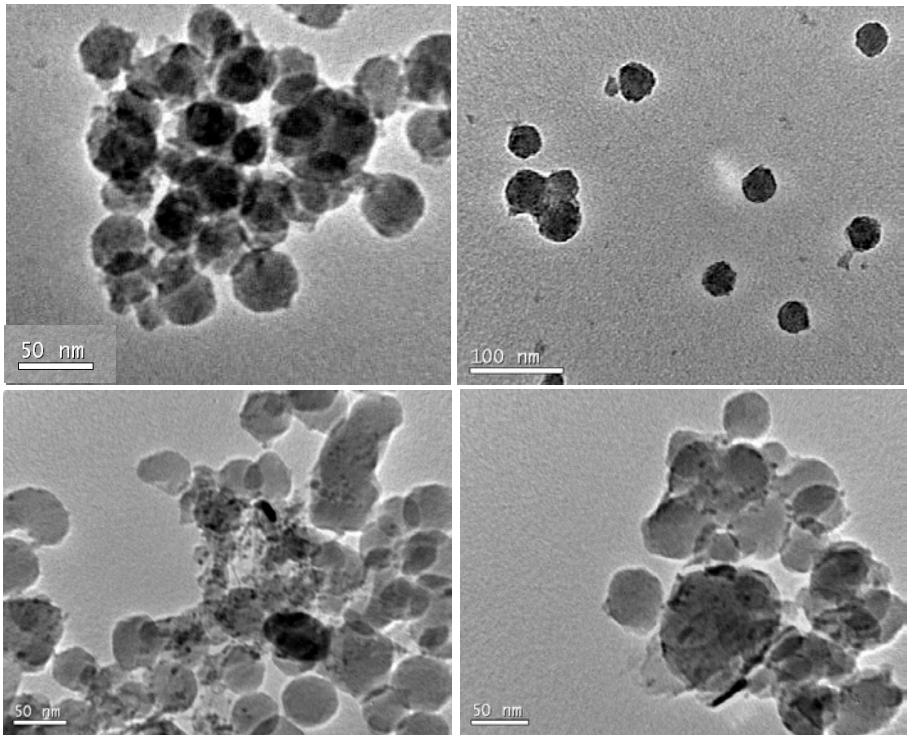

Figure 23**. TEM images of Ni-SiO_2 before (top two) and after (bottom two) reaction in CH_4 at 700ºC for 20 minutes**

3.2 CO-FEEDING TESTS OVER NON-HOLLOW AND HOLLOW NI@SIO_2

After studying the impact of nanostructure on reaction and diffusion for the individual, unmixed reactants H_2 and CH_4, we next investigate how the co-feeding of both reactant gases (H_2 and CH_4) affects the conversion and diffusion of each component.

As before, the respective nanostructured catalyst material is inserted into a quartz glass tube with 5 mm in diameter. The nhNi@SiO_2 and hNi@SiO_2 (with 10nm in thickness) is first oxidized in air at 500ºC for 30 minutes to assure that the nickel nanoclusters are fully oxidized.

After that, mixed feeds of 25vol% H_2 and 25vol% CH_4 (balance He) were fed over each sample respectively.

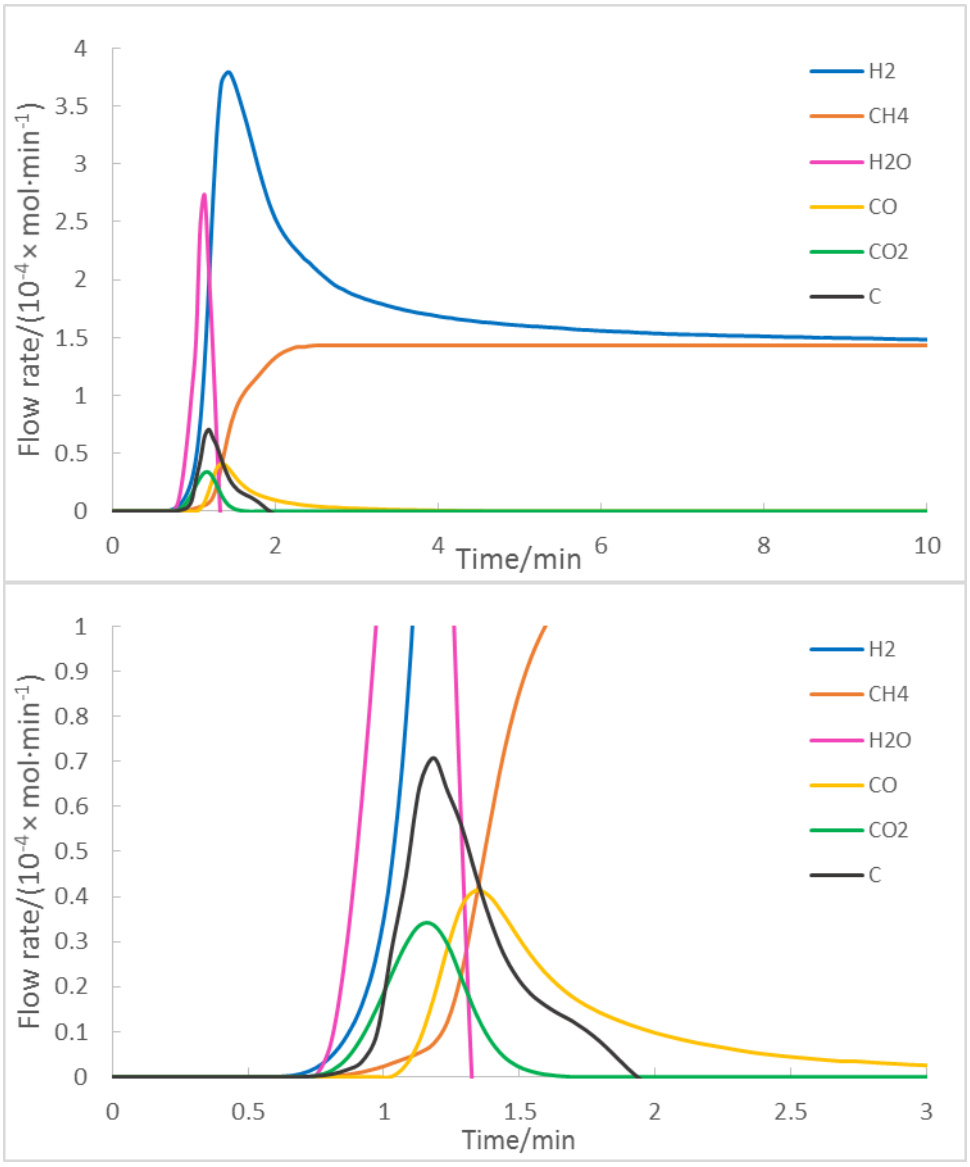

Figure 24. Co-feeding H_2 and CH_4 over nhNi@SiO_2 at 700°C. Catalyst weight = 0.2g (5.3wt.%Ni loading), feed stream : 3.125 cm^3/min H_2 + 3.125 cm^3/min CH_4 + 6.25 cm^3/min He. The bottom graph is the enlarged view that allows to see the occurrence of the minor reaction products.

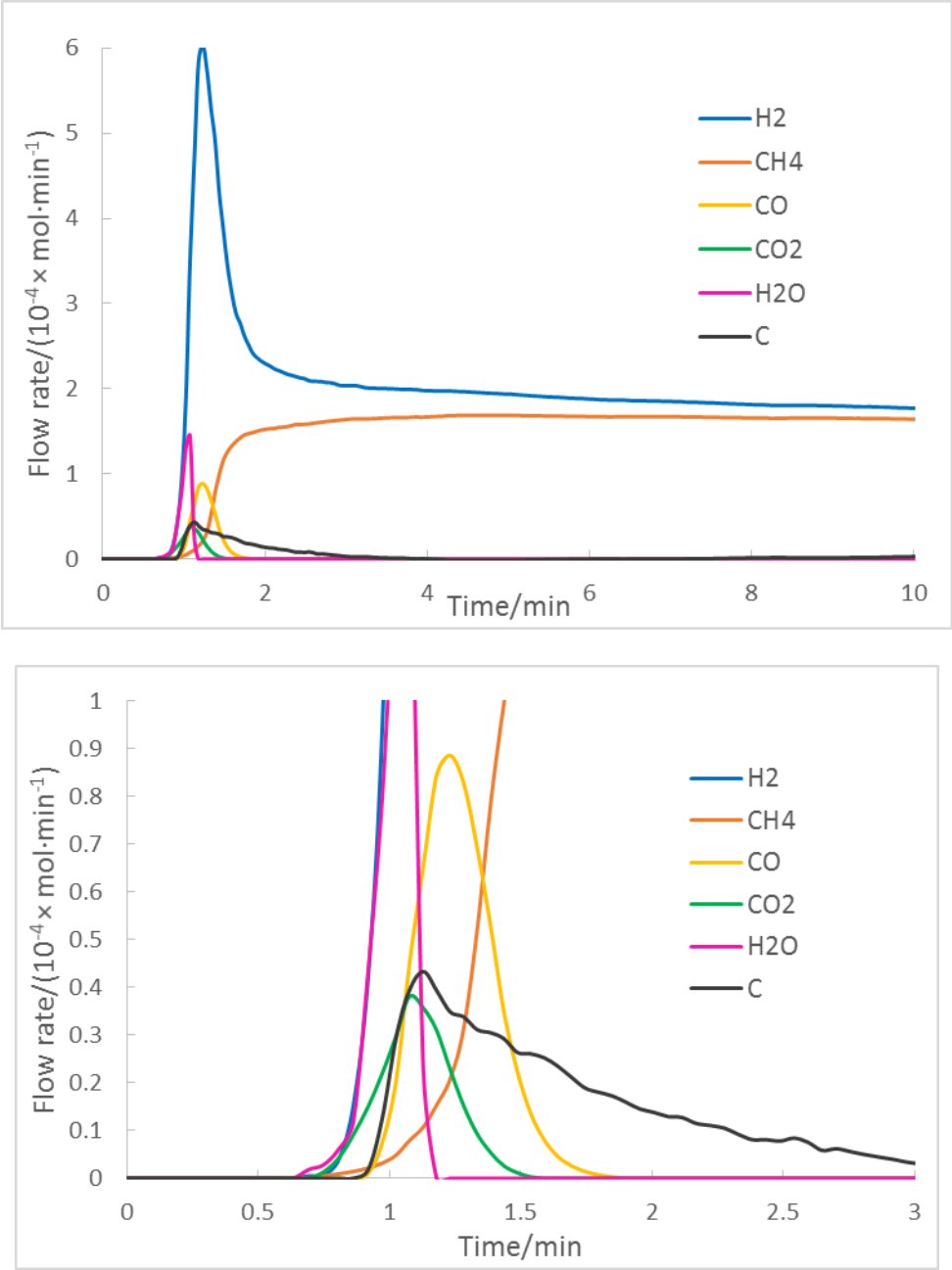

Figure 25. Co-feeding H_2 and CH_4 over hNi@SiO_2 at 700°C. Catalyst weight = 0.2g (4.6wt%Ni loading), feed stream: 3.125 cm^3/min H_2 + 3.125 cm^3/min CH_4 + 6.25 cm^3/min He. The bottom graph is the enlarged view that allows to see the occurrence of the minor reaction products.

Figures 24 and 25 show the product stream composition (as volumetric flows) versus time for H_2 and CH_4 co-feeds over nhNi@SiO_2 (fig. 24) and hNi@SiO_2 (fig. 25), respectively.

As before, we see in both cases the formation of H_2, CO, CO_2 and water as product of the rapid reactions of H_2 and CH_4 with the NiO cores. After a few minutes, product formation stops, indicating that the oxygen reservoir in the NiO nanoclusters has been exhausted. Compared with nhNi@SiO_2, hNi@SiO_2 has more controllable configuration with uniform diffusion pathways, so we again observe that the reactions over nhNi@SiO_2 were smear out shown in Figure 24.

A striking difference in the results from the mixed feed to the unmixed feed is the much stronger temporal off-set between CO_2 and CO as oxidation products. While for the unmixed methane feed both CO_x products overlapped in their occurrence virtually entirely (more specifically, CO_2 formation was almost entirely "enclosed" by the much longer and more pronounced CO formation), in the co-fed case we observe a much more pronounced CO_2 formation which precedes the CO formation significantly and decays rapidly as soon as CO formation sets on. This suggests that water-gas shift plays a significant role in the co-fed system: Based on the results from the individual feed, we expect that the faster H_2 diffusion to result in steam formation before any significant degree of methane conversion occurs. Hence, any CO that is formed from methane oxidation encounters an atmosphere with an enhanced water partial pressure, and is hence converted to CO_2 (forming H_2 as co-product at the same time). Hence, we also observe that CO evolution starts in coincidence with the CO_2 maximum, in agreement with WGS as a major contributor to CO_2 formation.

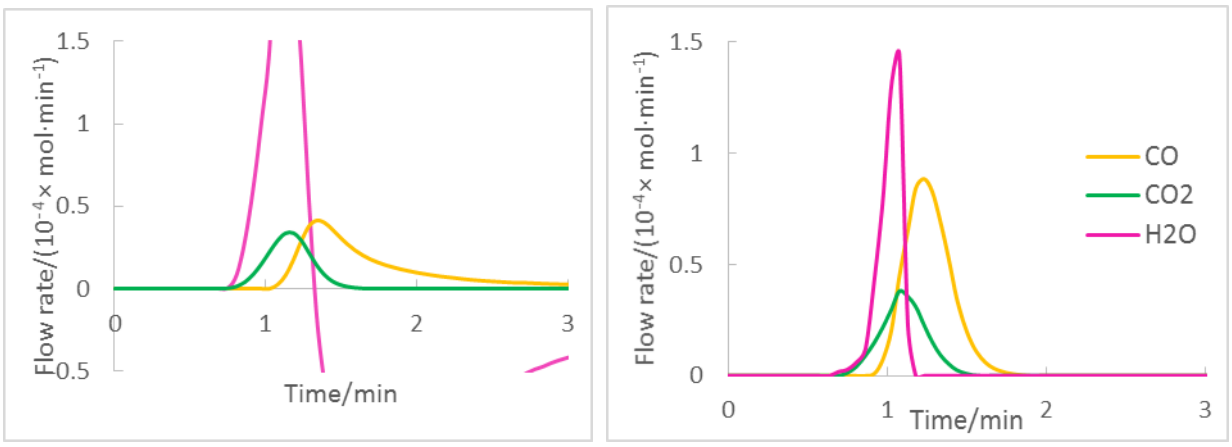

Figure 26. CO and CO_2 flow rates on nhNi@SiO_2 and hNi@SiO_2 in co-fed experiments

Comapring CO and CO_2 flow rates for nhNi@SiO_2 and hNi@SiO_2, respectively, (see fig. 26) we observe that CO_2 formation curves for both cases look similar (and symmetrical) in shape while CO formation curves are quite different. Figure 26 shows the negative water flow rate from time ~1.3 min, which is consistent with the slower decline of CO signal after maximum formation. Therefore, the long trailing end of CO signal in nhNi@SiO_2 is mostly likely the result of steam, which is formed on some particles on the inside of the particle, encountering coked particles on the way out and gasifying the carbon, resulting in CO and H_2.

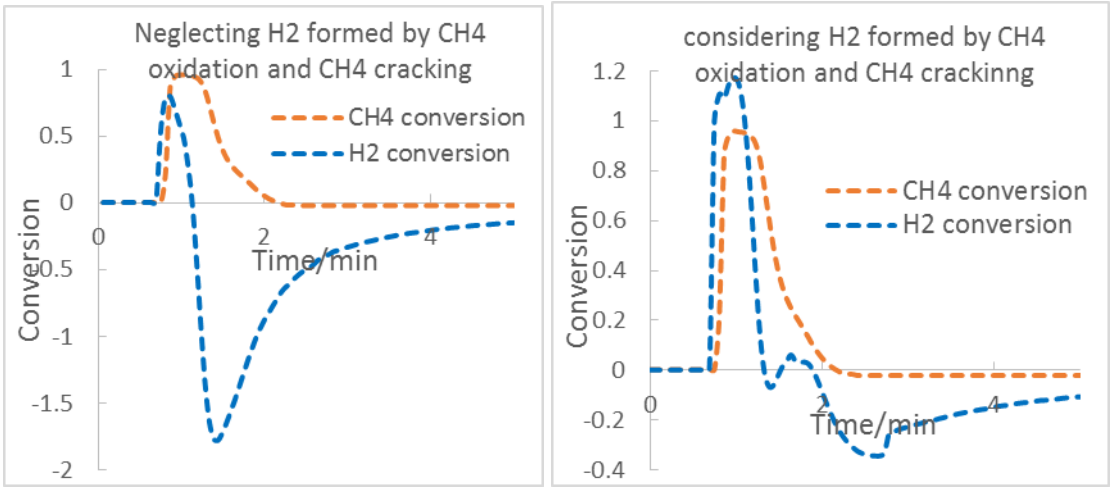

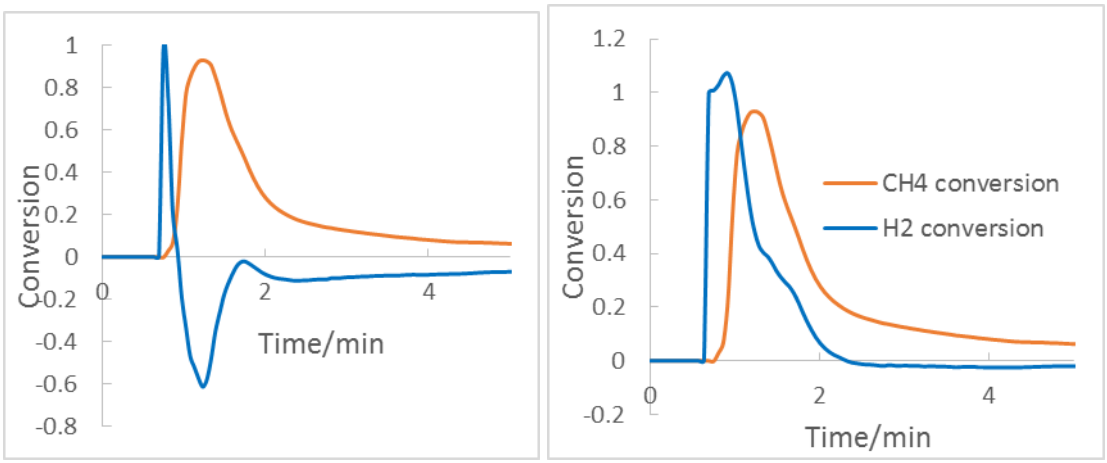

Figure 27. Conversion of CH_4 and H_2 over nhNi@SiO_2 (top two) and hNi@SiO_2 (bottom two) in co-fed experiments

A key complexity in the co-fed experiments is the fact that hydrogen is not only a reactant but also the product from methane partial oxidation and methane cracking. Due to the lack of independent information about H_2 consumption via oxidation and H_2 formation from methane conversion, it is impossible in this system to determine the actual H_2 conversion. In an attempt to circumvent this problem, we calculate two "extreme" scenarios under two different approximate assumptions: In the first case, we assume that H2 formed from CH4 partial oxidation as well as CH_4 cracking is negligible (knowing well that this assumption is not correct!) (see fig. 27 (left)), and in the second case, we assume that the methane conversion is not significantly affected by the presence of the H_2 co-feed and the we hence can take the H_2 formation from the unmixed case (see fig.27 (right)) and subtract it from the observed H_2 flow to obtain the hydrogen conversion. (The detailed calculations can be found in Section 1.01(a)(i)A.3). However, the fact that we obtain negative H_2 conversions for all cases indicates that the two reaction systems are intricately interlinked (as one would expect) and either assumption introduces too large errors to result in usable conversion curve for H_2. On both

materials, H_2 conversion precedes CH_4 conversion. This is more pronounced on hollow material, which indicates that a silica shell with uniform thickness can result in selectivity.

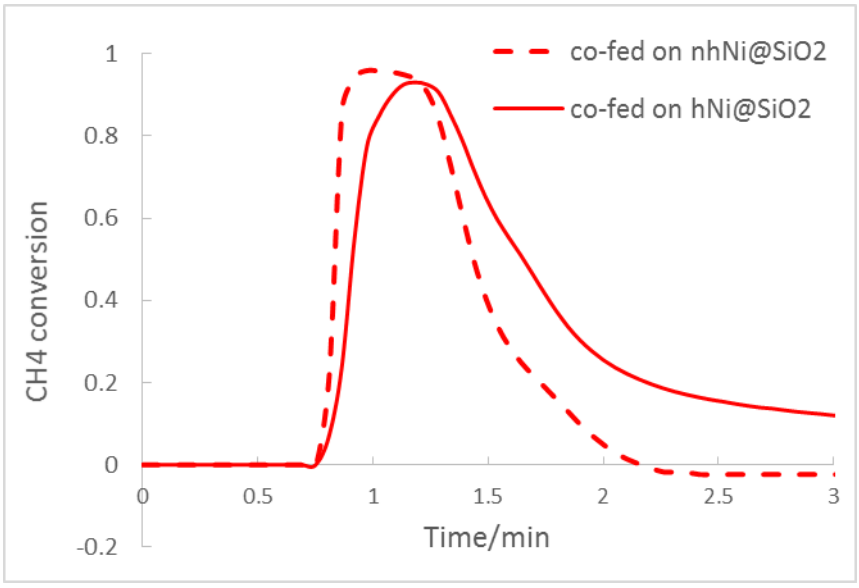

Figure 28. CH4 conversion on nhNi@SiO2 and hNi@SiO2 in co-fed experiments

Comparing CH_4 conversion on different nanostructure, as Figure 28 shows, CH_4 conversion curve on hollow material lags behind that on nhNi@SiO_2. This is a good indication that a uniform thicker shell can enhance the selective diffusion of H_2, which is the basis for our future work.

Table 2. Integral CH_4 conversion on hNi@SiO_2 and nhNi@SiO_2 in co-fed experiments

nhNi@SiO_2	hNi@SiO_2
0.64	0.85

Integral CH_4 conversion on hNi@SiO_2 and nhNi@SiO_2 in co-fed tests are summarized in Table 2. The integral CH_4 conversion on hNi@SiO_2 is much higher. As we discussed previously, more severe coking tends to occur in hollow material. Here again, the experiment results confirmed our speculation.

3.3 SUMMARY

Based on the results of oxidation of unmixed hydrogen and methane over nickel-silica core-shell materials, we were able to see the expected impact of diffusion through the porous silica shell on the conversion of H_2 and CH_4 with nickel oxide, suggesting that these materials might allow for selective conversion.

Different nanostructures of nhNi@SiO_2 and hNi@SiO_2 result in different reactions kinetics in these two materials. Diffusion pathway plays a significant role in kinetics. hNi@SiO_2 has a uniform diffusion pathway, while nhNi@SiO_2 has more complicated diffusion pathways, resulting in more secondary reactions.

H_2 can diffuse more easily than CH_4. Both in unmixed and mixed feed experiments, the H_2 conversion curve slightly preceded the CH_4 conversion curve on hollow material, reflecting that a uniform silica shell can contribute to a selective diffusion of H_2 through silica pores. However, the effect is very small and needs to be enhanced in order to make this difference useful for selective hydrogen conversion.

Since hNi@SiO_2 that has a uniform shell thickness is more controllable, it will be used for further study. It is likely that the selective diffusion hydrogen would be enhanced with an increased silica shell thickness. Further work will hence focus on hNi@SiO_2 with thicker silica shells.

4.0 SUMMARY AND OUTLOOK

4.1 SUMMARY

The porosity of the outer shell of nickel-silica core-shell allows it to have the similar function as selective membrane, and thus can be used to improve selectivity in certain reaction. Ideally, we desire to apply these metal-silica core-shell materials to selective dehydrogenation reactions to remove the produce hydrogen from the product mixture. Previously, other researchers [5] has reported their findings about a preferential oxidation of methane over iso-butane on silica-coated Pt. The porous structure of silica, which wrapped Pt metal particles, controlled selectivity in the catalytic reaction.

In our case, we apply nickel-silica core-shell materials to H_2 - CH_4 mixtures, where we expect a preferential diffusion of H_2 through the silica layer and hence a preferential conversion of H_2 over the metal cores inside the silica shell.

The reactive tests of nanostructured nickel-silica core-shell catalysts showed the anticipated impact of diffusion through the porous silica shell on the conversion of H_2 and CH_4 with nickel oxide, suggesting that these materials might allow for selective conversion. Different nanostructures result in different kinetics due to different diffusion pathways, which plays a significant role in kinetics. nhNi@SiO_2 has more complicated diffusion pathways, while hNi@SiO2 has a uniform diffusion pathway.

H_2 can diffuse more easily than CH_4. This is supported by the observation that in unmixed tests, H_2 conversion curve slightly precedes CH_4 conversion curve on hNi@SiO_2, which is caused by the easier diffusion of H_2 through uniform silica shell; and in co-fed tests, CH_4 conversion on hNi@SiO_2 lags behind CH_4 conversion on nhNi@SiO_2, suggesting a shell with uniform diffusion length can result in selectivity.

Based on these observations, we conclude that the selective diffusion of H_2 in H_2-CH_4 mixtures through porous silica is detectable, but quite small, and therefore the materials need further tailoring. hNi@SiO_2 with a more controllable structure will be used for further study. One can expect to see enhanced selective hydrogen diffusion with increasing thickness of the silica shell. Our future work will focus on hNi@SiO_2 with thicker shell.

4.2 OUTLOOK

4.2.1 Preferential oxidation of H_2 to CH_4 on hNi@SiO_2 with thicker shell

The reactive tests of nanostructured nickel-silica core-shell catalysts showed the anticipated impact of diffusion through the porous silica shell on the conversion of H_2 and CH_4 with nickel oxide. For hNi@SiO_2 with 10 nm shell thickness, the preferential diffusion of H_2 is detectable, but quite small. It is expected to observe the “selective” diffusion of H_2 to be enhanced via increasing the thickness of silica shell. By increasing the silica shell thickness, the diffusion distance can be increased so that the tendency of preferential diffusion of H_2 can be enhanced.

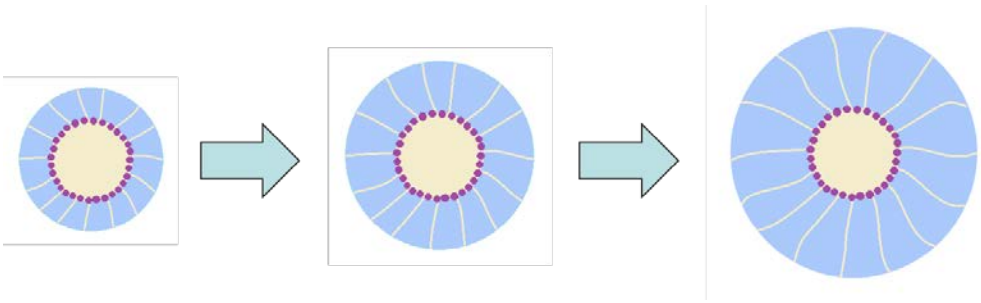

Figure 29. Illustrations of hNi@SiO_2 with different silica shell thickness

In general, there are three ways to control silica shell thickness in silica-based hollow core-shell materials: control of reaction time, TEOS amount, and/or ammonia concentration. The silica-particle growth is reaction-control by the slow hydrolysis of TEOS rather than fast TEOS condensation [19]. The overall reaction for TEOS hydrolysis and condensation is as follows:

$$Si(OC_2H_5)_4 + 2H_2O \rightarrow SiO_2 + 4C_2H_5OH$$

Where water serves as a reactant for TEOS hydrolysis, and stabilizes micelles in the reverse microemulsion system.

The silica shell growth is first order with respect of TEOS concentration and the apparent rate constant for silica-particle growth (k_c) is determined via the following equation [18]:

$$1-\frac{V_p(t)}{V_p(\infty)}=\exp(-k_c t)$$

Where k_c is the rate constant for silica-particle growth; $V_p(t)$ and $V_p(\infty)$ are the volume of silica particles at time t and at the end of reaction.

4.2.1.1 Reaction time

The silica-particle growth equation indicates the silica shell thickness as a function of reaction time. Whaley [8] in our group has previously reported the silica shell growth is time dependent, in which the particle growth is rapid during initial reaction period and then levels off.

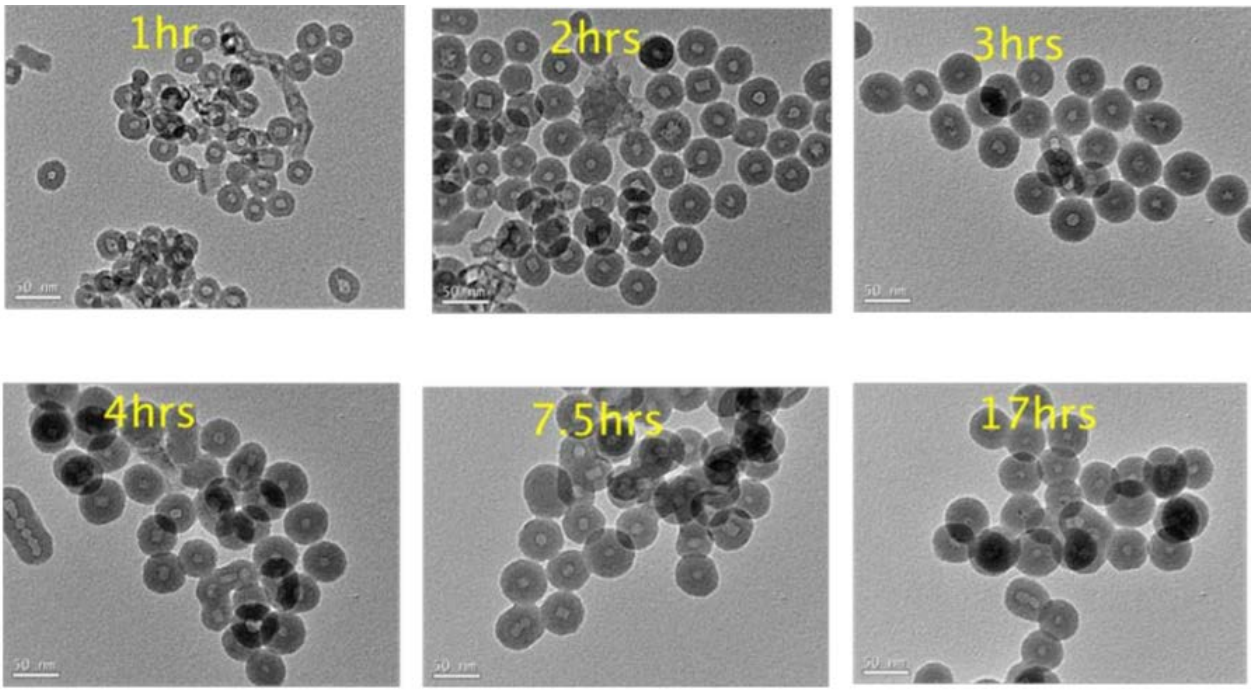

Figure 30. TEM images of hNi@SiO_2 with different reaction times (using 20g TEOS) [8]

Figure 30 shows an example of the growth of silica shell as a function of reaction time. It was observed that shell thickness increased as a function of time at initial stage while the cavity dimension was constant (fig. 30). After 7.5 hours, the shell thickness is independent of the reaction time due to the insufficient availability of water, which not only serves as a reactant for TEOS hydrolysis, but also stabilizes micelles in the reverse microemulsion system.

4.2.1.2 TEOS amount

TEOS amount is another way to adjust the thickness of silica shell. Whaley [8] reported that the silica shell thickness increases with the increasing of TEOS amount from 1g to 10g (fig. 31). Further growth of silica shell requires the availability of water.

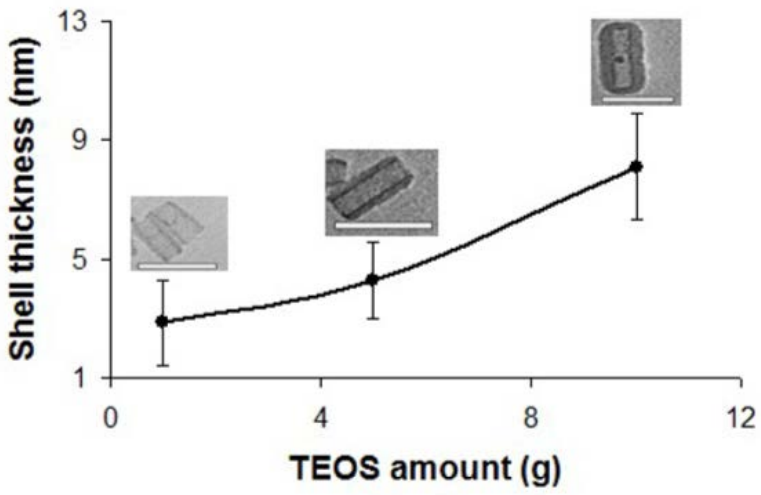

Figure 31. Silica shell thickness versus TEOS amount. Synthesis condition: reaction time 1hr, 3mL 16.5M ammonia solution [8]

4.2.1.3 Ammonia concentrations

The ammonia serves as a catalyst for TEOS hydrolysis, a higher concentration will facilitate hydrolysis process. Whaley [8] reported that the silica shell thickness increases initially with increasing ammonia concentrations, reaching a plateau above the ammonia concentration of 4mol/L. However, the growth of silica shell is limited by the availability of both water and TEOS amount and hence eventually will slow down, as it shown in Figure 32.

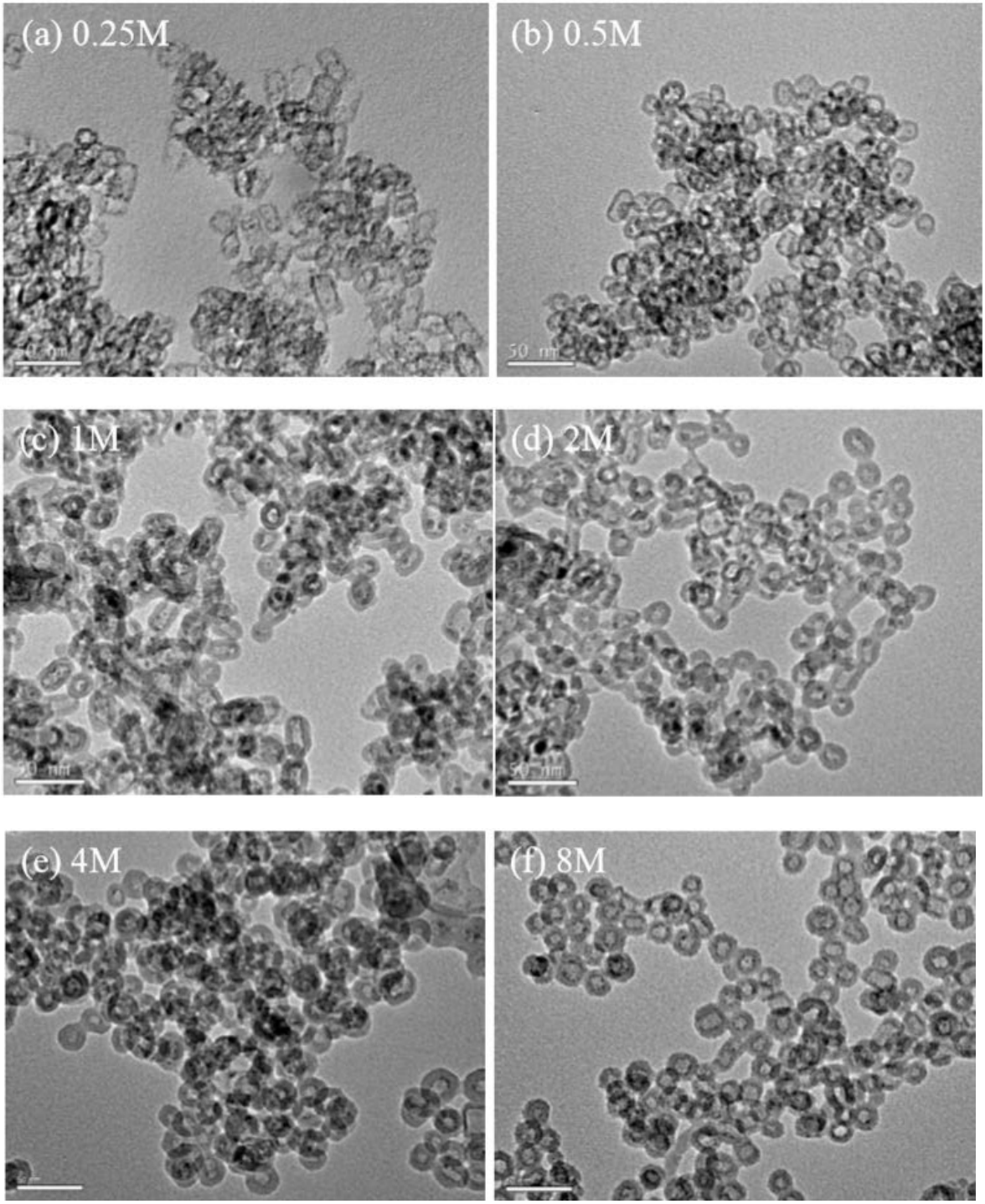

Figure 32. TEM images of Ni@SiO2 synthesized using different ammonia concentrations (a-f) [8]

4.2.2 Potential application of core-shell catalysts in chemical looping process

The significance of core-shell nanostructures is not merely its application in this specific selective diffusion of hydrogen versus methane. We would like to investigate the preferential oxidation of hydrogen versus ethane, propane, or heavier hydrocarbons as we expect that the selective diffusion of hydrogen versus other hydrocarbons will be enhanced as the molecular weight difference between the hydrocarbons and hydrogen becomes larger. Ultimately, we desire to apply these materials dehydrogenation reactions in chemical looping processes.

The concept behind this idea can be explained using catalytic methane dehydroaromatization (DHA) as an example. Methane DHA is the non-oxidative conversion of methane to benzene and hydrogen with the aid of a catalyst. The reaction formula is as follows:

$$6CH_4(g) \rightarrow C_6H_6(g)+9H_2(g),\ \triangle G_r^o = +433\text{kJ/mol},\ \triangle H_r^o = +531\text{kJ/mol}$$

Mo/HZSM-5 is the most widely studied catalyst for this reaction [20, 30, 31]. However, the methane conversion of this reaction is thermodynamically limited to very low conversions, about 10% at a typical reaction temperature of 700^{o}C. One way to increase the methane conversion is by continuously removing hydrogen so that the reaction can be pulled towards the formation of benzene ("product pull"). This has been widely studied with the use of membrane reactors with hydrogen selective membranes. For example, Iliuta et al. [15] studied methane DHA in a membrane reactor, shown in Figure 33. In this reactor, hydrogen can permeate through the selective membrane made from Pd/Ag alloy and then diffuse out of the system. However, membrane reactors are hampered by high cost due to the fact that almost all H_2 selective membranes rely on Pd-based membranes, and the quality of the membrane imposes extreme

demands on the production. Furthermore, all studies of DHA to-date show major problems due to coking, which is strongly enhanced upon removal of hydrogen.

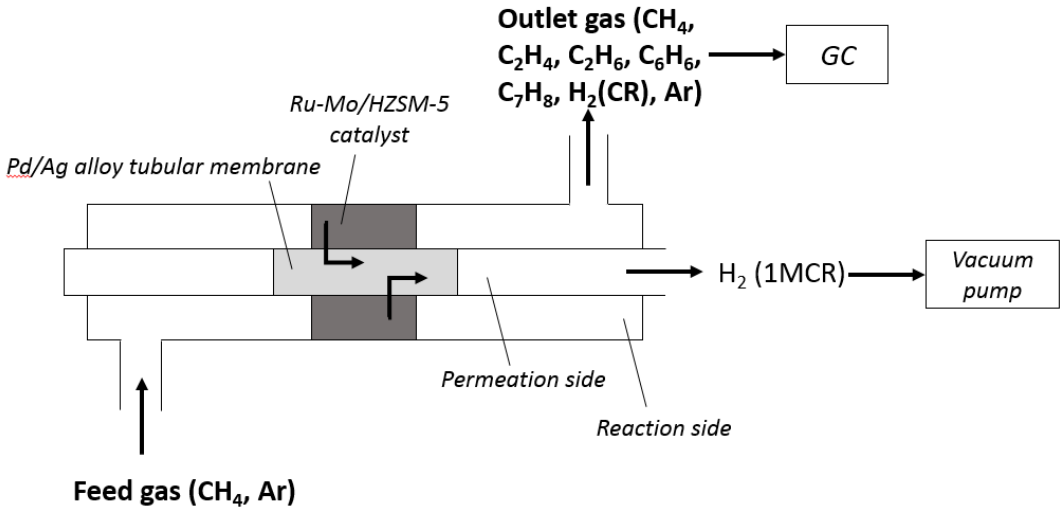

Figure 33. Schematics of membrane reactor for methane dehydro-aromatization reaction [15]

The direct aromatization of methane to benzene first requires an initial activation of CH_4 molecule. CH_4 is activated on the metal sites forming CH_x species, which dimerize to C_2H_y. Then, subsequent oligomerization on the acidic sites located inside the zeolite channels yields benzene and naphthalene, as well as copious amounts of coke [25, 26].

In this mechanism, coke is formed in two ways: (a) from dehydrogenated methane (‘‘CH_x’’) in parallel with the desired C–C bond formation step, and (b) from lower intermediates (e.g., C_2H_y in fig. 34) in series with the formation of the desired product benzene or other aromatics.

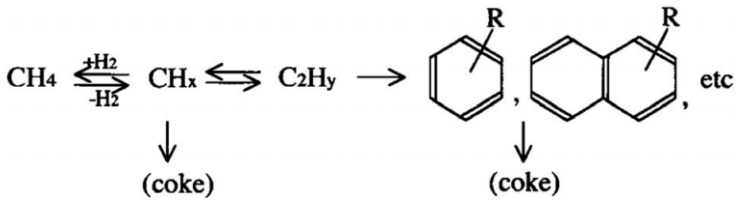

Figure 34. Mechanism for the formation of aromatics and coke in DHA reaction [25]

We are proposing a fundamentally different approach: Instead of using membrane reactor, we conceive to apply the hollow $Ni@SiO_2$ to methane DHA with $hNi@SiO_2$ as the selective membrane to consume hydrogen, i.e. we propose to use the hollow core-shell structures as "internal nano-membrane reactors" which selectively remove and convert the hydrogen from the reactant/product mixture. This concept would require a periodic re-oxidation of the $Ni@SiO_2$ materials and hence result in a "Chemical looping" type process operation.

"Chemical looping" is a term used for a periodic process operation in which a material is used to transport oxygen from one reaction half-step to the second half-step. It is most commonly (in fact, almost exclusively to-date) applied to combustion: Chemical looping combustion (CLC) typically employs a dual fluidized bed system where a metal oxide is employed as a bed material providing the oxygen for combustion in the fuel reactor. This result in the reduction of the metal oxide and the reduced metal is then transferred to a second reactor (the "air reactor") and re-oxidized before being re-introduced back to the fuel reactor, thus completing the loop [16]. The schematics of chemical looping combustion processes is shown in Figure 35.

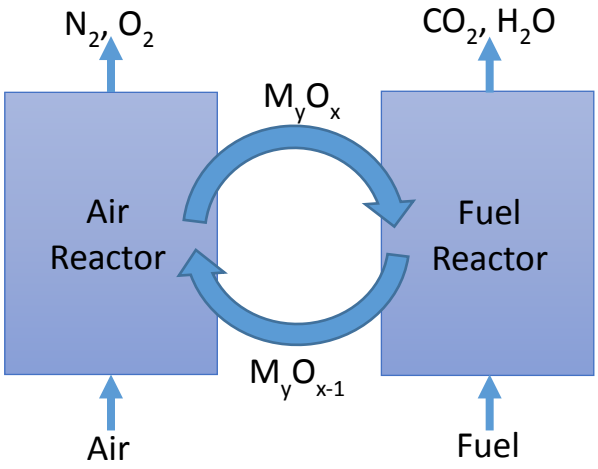

Figure 35. Schematics of chemical looping combustion processes

For methane DHA in a chemical looping configuration, the fuel reactor will be packed with the catalyst for methane dehydroaromatization (such as Mo/HZSM-5) and an oxidized hNi@SiO_2. When flowing methane over the fuel reactor, methane DHA and hydrogen oxidation (by NiO) are expected to occur simultaneously, forming (ideally) benzene and steam as reaction products. The involved reactions are as follows:

(1) $6CH_4(g) \rightarrow C_6H_6(g)+9H_2(g)$,

(2) $H_2(g)+NiO(s) \rightarrow H_2O(g)+Ni(s)$.

After the oxygen in nickel oxide has been entirely consumed, the system will be purged with inert gas, and then nickel can be re-oxidized to nickel oxide by flowing air. Note that this oxidation step is required for the reaction in any case as Mo/HZSM-5 is known to coke and deactive in methane DHA, requiring periodic coke burn-off. The proposed conept hence does not add an additional process steps, although the oxidative step will likely have to occur sooner and hence more frequently than in the conventional catalytic operation. Additionally, however, the formation of steam in the internal selective hydrogen oxidation is expected to result in a gasification of the coke during methane DHA and hence reduced deactivation of the catalyst. The introduction of the Ni@SiO_2 material would hence result in two beneficial effects.

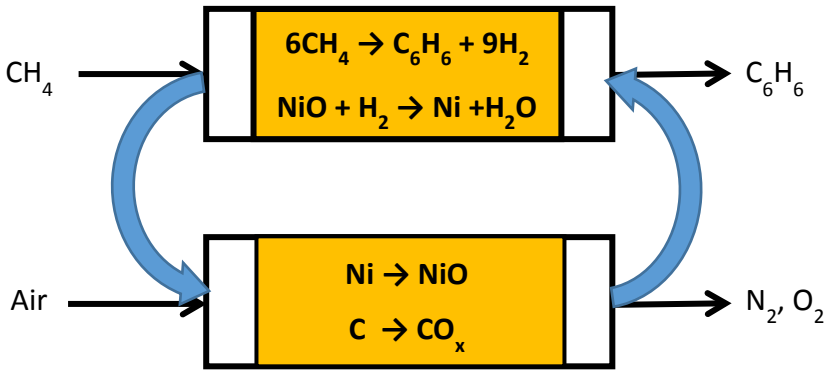

Figure 36. Schematics of CH_4 DHA in chemical looping process

Based on our observation, preferential diffusion of hydrogen versus methane does occur in the hNi@SiO_2 materials, but the difference is quite small and likely not sufficient to support the proposed concept. However, as mentioned above, we expect the selectivity to be greatly enhanced by increasing the shell thickness for the core-shell materials.

A second, different way to increase the selectivity is to combine the diffusive selectivity with a reactive selectivity, i.e. replace NiO with other metal oxides that show high reactivity with hydrogen but poor reactivity with methane. Our recent work in chemical looping combustion has shown that iron is such a material [27, 28]. We hence aim to replace the Ni clusters in the silica shells with Fe clusters and hence strongly enhance the selectivity of hydrogen oxidation vs methane conversion.

We expect to see this promising core-shell oxygen carrier that possesses reaction selectivity have a wider application in catalytic dehydrogenation reaction in the future.

APPENDIX A

CALCULATION IN REACTIONS

A.1 H_2 OXIDATION

When flowing hydrogen over nickel-based core silica shell materials, the reaction of H_2 oxidation would occur and the system would have following gas species: H_2, H_2O and He (inert gas), whose concentrations would be detected by the mass spectrometer at the outlet of the reactor. Hence the hydrogen conversion can be calculated from the concentrations (mole fraction y_i). The detailed calculation of mathematical procedure is laid out in the following.

$$H_2 + NiO \rightarrow H_2O + Ni$$

The total flow of moles entering the system (labeled 'in') is a parameter set in the experiment and is:

$$\dot{N}^{in} = \dot{N}^{in}_{H_2} + \dot{N}^{in}_{He}$$

The total number of molar flows exiting the system is:

$$\dot{N}^{out} = \dot{N}^{out}_{H_2} + \dot{N}^{out}_{He} + \dot{N}^{out}_{H_2O}$$

The inlet molar flows (set with the mass flow controllers) as well as the molar fractions y_i of the product gases (measured with the mass spectrometer) are known.

Since the flow rate of inert gas won't change after reaction, the actual total flow rate can be calculated based on the concentration of inert gas:

$$\dot{N} = \frac{\dot{N}_{\mathrm{He}}^{in}}{y_{\mathrm{He}}}$$

And hence hydrogen conversion can be defined as:

$$X_{\mathrm{H_2}} = \frac{\dot{N}_{\mathrm{H_2}}^{in} - \dot{N}_{\mathrm{H_2}}^{out}}{\dot{N}_{\mathrm{H_2}}^{in}} = \frac{\dot{N}_{\mathrm{H_2}}^{in} - y_{\mathrm{H_2}}\dot{N}}{\dot{N}_{\mathrm{H_2}}^{in}} \quad \square$$

A.2 CH_4 OXIDATION

When flowing methane over nickel-based core silica shell materials, there are several reactions going on and the system would have following gas species: H_2, CH_4, H_2O, CO, CO_2 and He (inert gas), whose concentrations would be detected by the mass spectrometer at the outlet of the reactor. The detailed calculation of mathematical procedure is laid out in the following.

$$\mathrm{CH_4 + 4NiO \rightarrow CO_2 + 2H_2O + 4Ni}$$

$$\mathrm{CH_4 + NiO \rightarrow CO + 2H_2 + Ni}$$

$$\mathrm{CH_4 \rightarrow C + 2H_2}$$

The total flow of moles entering the system (labeled 'in') is a parameter set in the experiment and is:

$$\dot{N}^{in} = \dot{N}_{\mathrm{CH_4}}^{in} + \dot{N}_{\mathrm{He}}^{in}$$

The total number of molar flows exiting the system is:

$$\dot{N}^{out} = \dot{N}^{out}_{H_2} + \dot{N}^{out}_{H_2O} + \dot{N}^{out}_{CH_4} + \dot{N}^{out}_{He} + \dot{N}^{out}_{CO} + \dot{N}^{out}_{CO_2}$$

The inlet molar flows (set with the mass flow controllers) as well as the molar fractions yi of the product gases (measured with the mass spectrometer) are known.

Since the flow rate of inert gas won't change after reaction, the actual total flow rate can be calculated based on the concentration of inert gas:

$$\dot{N} = \frac{\dot{N}^{in}_{He}}{y_{He}}$$

And hence methane conversion can be defined as:

$$X_{CH_4} = \frac{\dot{N}^{in}_{CH_4} - \dot{N}^{out}_{CH_4}}{\dot{N}^{in}_{CH_4}} = \frac{\dot{N}^{in}_{CH_4} - y_{CH_4}\dot{N}}{\dot{N}^{in}_{CH_4}} \square$$

CO selectivity and CO_2 selectivity can be defined as:

$$S_{CO} = \frac{\dot{N}_{CO}}{\dot{N}_{CH_4} - \dot{N}^{out}_{CH_4}}, \; S_{CO_2} = \frac{\dot{N}_{CO_2}}{\dot{N}_{CH_4} - \dot{N}^{out}_{CH_4}}$$

"Production rate" of carbon is calculated based on carbon balance:

$$\dot{N}^{in}_{CH_4} = \dot{N}^{out}_{CH_4} + \dot{N}^{out}_{CO} + \dot{N}^{out}_{CO_2} + \dot{N}^{out}_{C}$$

A.3 CO-FEEDING H_2 AND CH_4

Figure 37. Illustration of inlet and outlet of co-feeding H_2 and CH_4 over $Ni@SiO_2$

When co-feeding hydrogen and methane over $Ni@SiO_2$, the following reactions would happen:

$$H_2 + NiO \rightarrow H_2O + Ni$$

$$CH_4 + 4NiO \rightarrow CO_2 + 2H_2O + 4Ni$$

$$CH_4 + NiO \rightarrow CO + 2H_2 + Ni$$

$$CH_4 \rightarrow C + 2H_2$$

In co-feeding run, hydrogen is not only the reactant but also the product from methane partial oxidation and methane cracking. In addition, we can't determine how much H_2 were generated from CH_4 oxidation reaction and CH_4 cracking. Hence it's almost impossible to calculate the actual H_2 conversion. So we gave our calculations in two extreme scenarios: one neglecting the H_2 formed from CH_4 partial oxidation as well as CH_4 cracking, and the other taking the H_2 formed from CH_4 oxidation into consideration.

- Scenario 1 (neglecting H_2 formed by CH_4 oxidation and CH_4 cracking):

$$X_{H_2} = \frac{\dot{N}_{H_2}^{in} - \dot{N}_{H_2}^{out}}{\dot{N}_{H_2}^{in}} = \frac{\dot{N}_{H_2}^{in} - y_{H_2}\dot{N}}{\dot{N}_{H_2}^{in}},$$

$$X_{\mathrm{CH_4}} = \frac{\dot{N}^{in}_{\mathrm{CH_4}} - \dot{N}^{out}_{\mathrm{CH_4}}}{\dot{N}^{in}_{\mathrm{CH_4}}} = \frac{\dot{N}^{in}_{\mathrm{CH_4}} - y_{\mathrm{CH_4}}\dot{N}}{\dot{N}^{in}_{\mathrm{CH_4}}},$$

This calculation would give us large negative value of H_2 conversion.

- Scenario 2 (considering H_2 formed by CH_4 oxidation and CH_4 cracking):

$$X_{\mathrm{H_2}} = \frac{\dot{N}^{in}_{\mathrm{H_2}} - \dot{N}^{out}_{\mathrm{H_2}}}{\dot{N}^{in}_{\mathrm{H_2}}} = \frac{\dot{N}^{in}_{\mathrm{H_2}} - y_{\mathrm{H_2}}{}'\dot{N}}{\dot{N}^{in}_{\mathrm{H_2}}},$$

$$X_{\mathrm{CH_4}} = \frac{\dot{N}^{in}_{\mathrm{CH_4}} - \dot{N}^{out}_{\mathrm{CH_4}}}{\dot{N}^{in}_{\mathrm{CH_4}}} = \frac{\dot{N}^{in}_{\mathrm{CH_4}} - y_{\mathrm{CH_4}}\dot{N}}{\dot{N}^{in}_{\mathrm{CH_4}}},$$

where $y_{H2}{}'$ was obtained by y_{H2} subtracting the H_2 concentration corresponding to H_2 signal data in another experiment in which 25% CH_4 was run over Ni@SiO_2.

"Production rate" of carbon is calculated based on carbon balance:

$$\dot{N}^{in}_{\mathrm{CH_4}} = \dot{N}^{out}_{\mathrm{CH_4}} + \dot{N}^{out}_{\mathrm{CO}} + \dot{N}^{out}_{\mathrm{CO_2}} + \dot{N}^{out}_{\mathrm{C}}$$

APPENDIX B

SYNTHESIS

B.1 SYNTHESIS OF NI-SiO_2

Pure silica particles are synthesized following the same reverse microemulsion route described in section 2.1.1 without the addition of nickel nitrate solution as the only difference. The dried white power sample is calcined in the air at 500°C for 2 hours to remove the surfactants as described in section 2.1.2. 0.6g above silica nanoparticles are dispersed in 15mL DI water by sonication. The $NiCl_2$ solution is prepared by dissolving 0.4 g $NiCl_2$ in 10 mL DI water. A mixture of the above $NiCl_2$ solution and the silica nanoparticles are sonicated for better dispersion for 20min. Ammonium hydroxide is then added dropwise (~3-5mL) until the pH of the solution is ~9.5. Afterwards, the solution is mixed for another 20min, and then centrifuged and dried. The dried sample is calcined at 300°C in the air for 2 hours. (The procedure is developed by M. Najera.)

APPENDIX C

REACTIVITY TEST SET-UP

During the reactive test, it is observed that the CH_4 signal at 700°C preceded the signal at room temperature when feeding CH_4 over nickel-silica core-shell materials. To investigate the reason for the noticeable signal delay at room temperature, three sets of experiments were conducted, varying the flow rates of CH_4 and inert gas. Figure 10 shows one of these experiments in which 25vol%CH_4 (diluted with argon) are fed over nhNi@SiO_2 sample at 700°C. A ~10 s delay of the CH_4 signal vs the signal at room temperature was observed.

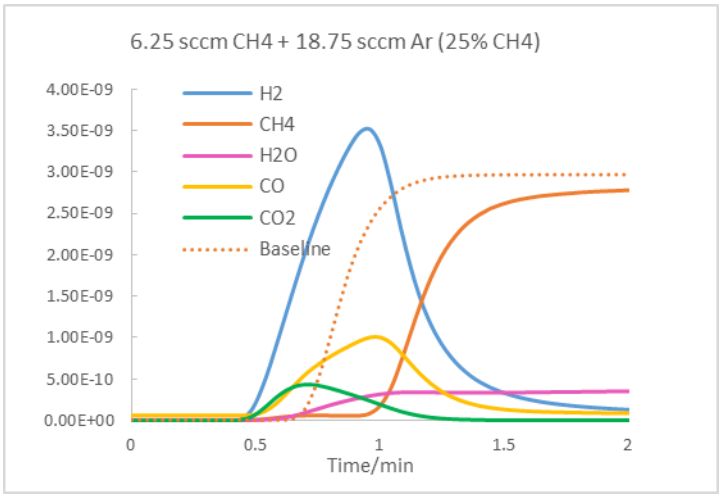

Figure 38. Feeding 25% CH_4 over nhNi@SiO_2. The dotted line shows the CH_4 signal during flow at room temperature. Solid lines are for 700°C and show methane along with the main reaction products.

The theoretical time required for signal breakthrough after opening the feed stream can be calculated through measuring the volume of the feed lines and the reaction system which is about 14 cm^3. For CH_4 oxidation reaction, one mole CH_4 can generation one mole CO and two moles H_2, or one mole CO_2 and two moles H_2O, so in either case, the volumetric flow rate is tripled after complete reaction. Another reason for volume change is the temperature change. Assuming ideal gas behavior, at 700°C, the volume of gas will become 3.5 times larger than that at room temperature. Hence, the volume change from room-temperature feed conditions to effluent gases after reaction at 700°C can estimated for the present system to be ~10. The equations are established as follows:

- At room temperature (RT), $t = \dfrac{V_{FR}}{Q_{CH4} + Q_{Ar}}$ (1)
- At 700°C, $t = \dfrac{V_{FR1}}{1.5(Q_{CH4} + Q_{Ar})} + \dfrac{V_{FR2}}{3.5(Q_{CH4} + Q_{Ar})} + \dfrac{V_{FR3}}{10Q_{CH4} + 3.5Q_{Ar}}$ (2)

At room temperature, the theoretical time required for signal breakthrough can be obtained by equation (1), in which 14 (cm^3) is the volume of the reaction system from mass flow controller to mass spectrometer ad Q_i is the flow rate of component i.

At 700°C, in the first term, V_{FR1}(cm^3) is the volume of line from mass flow controller to the entrance of reactor. At this point, the temperature is ~180°C, so the volumetric flow rates become 1.5 times larger than the initial condition. For the second term, V_{FR2} (cm^3) is the volume from entrance of the reactor to the catalyst zone. No reaction happens yet; volumetric flow rate should increase 3.5-fold due to 700°C environment in the reactor. As to the last term, V_{FR3}(cm^3) is the volume from catalyst zone to mass spectrometer. After reaction, the volumetric flow rate of CH_4 should increase by a factor of 10 which accounts for the volumetric change after reaction

and temperature change (from room temperature to 700ºC), and the volumetric flow rate of argon should increase 3.5-fold, which only resulted from temperature change.

The following table shows that the time calculated by equations for signal breakthrough and the time measured in the experiments generally are in good agreement, which supports the explanation that it is volumetric change and temperature change that result in the preceding signal breakthrough at reaction temperature.

Table 3. Comparison of time calculated for signal breakthrough and time measured with different volumetric flow rate

Volumetric Flow Rate/(sccm)		Time Calculated/(min)		Time measured/(min)	
CH4	Argon	At RT	At 700ºC	At RT	At 700ºC
6.25	6.25	1.12	0.56	1.1	0.63
2.08	6.25	1.68	0.87	1.5	0.83
0.69	6.25	2.02	1.10	1.8	1.2
6.25	18.75	0.56	0.29	0.58	0.43

BIBLIOGRAPHY

1. R. G. Chaudhuri et al. Core/Shell Nanoparticles: Classes, Properties, Synthesis Mechanisms, Characterization, and Applications. *Chem. Rev.*, 2012, *112* (4), pp 2373–2433.

2. S. H. Joo, J. Y. Park, C-K Tsung et al. Thermally stable Pt/mesoporous silica core-shell nanocatalysts for high-temperature reactions. *Nature Materials* 8 (2009), 126-131.

3. Somorjai, G. A. & Rioux, R. M. High technology catalysts towards 100% selectivity. Fabrication, characterization and reaction studies. *Catal. Today* 100 (2005), 201–215.

4. B.J. Jankiewicz, D. Jamiola et al. Silica–metal core–shell nanostructures. *Advances in Colloid and Interface Science* 170 (2012), 28-47.

5. K. Hori et al. Preparation of silica-coated Pt metal nanoparticles using microemulsion and their catalytic performance. *Science and Technology of Advanced Materials* 7 (2006), 678–684.

6. Breck, D.W. (Eds). Zeolite Molecular Sieves: Structure, Chemistry and Use, John Wiley & Sons, New York, 1974.

7. Clifford K. Ho and Stephen W. Webb (Eds). Gas Transport in Porous Media. Springer, the Netherlands, 2006.

8. L. Whaley Synthesis and Evaluation of Metal-Silica Core-Shell Nanomaterials for Catalysis. Doctoral Dissertation, University of Pittsburgh, 2012.

9. Liz-Marzan, L.M., M. Giersig, and P. Mulvaney, Synthesis of Nanosized Gold-silica Core-shell Particles. *Langmuir*, 1996. 12 (18): p. 4329-4335.

10. J.C. Park, et al., Ni@SiO2 yolk-shell nanoreactor catalysts: High temperature stability and recyclability. *Journal of Materials Chemistry*, 2010. 20(7): p. 1239.

11. C. Graf, et al., A General Method to Coat Colloidal Particles with Silica. *Langmuir*, 2003. 19(17): p. 6693-6700.

12. S. Takenaka, et al., Structures of Silica-Supported Co Catalysts Prepared Using Microemulsion and Their Catalytic Performance for the Formation of Carbon Nanotubes

through the Decomposition of Methane and Ethylene. *The Journal of Physical Chemistry C*, 2007. 111(21): p. 7748-7756.

13. H. Matsune, et al., Network structure consisting of chain-like arrays of gold nanoparticles and silica layer prepared using a nonionic reverse-micelle template. *Journal of Nanoparticle Research*, 2006. 8(6): p. 1083-1087. 85.
14. K. Kamata, Y. Lu, and Y. Xia, Synthesis and Characterization of Monodispersed CoreShell Spherical Colloids with Movable Cores. *Journal of the American Chemical Society*, 2003. 125(9): p. 2384-2385.

15. Maria C. Iliuta, Bernard P et al., Methane Nonoxidative Aromatization over Ru-Mo/HZSM-5 at Temperatures up to 973 K in a Palladium-Silver/Stainless Steel Membrane Reactor. *Ind. Eng. Chem. Res*. 2003, 42, 323-330.

16. http://en.wikipedia.org/wiki/Chemical_looping_combustion

17. M. A. Malik et al. Microemulsion method: A novel route to synthesize organic and inorganic nanomaterials. *Arabian Journal of Chemistry* (2012) 5, 397-417.

18. C.-L.F.Chang, H. S. Fogler. Kinetics of silica particle formation in nonionic W/O microemulsions from TEOS. *Materials, Interfaces, and Electrochemical Phenomena* 1996. 42(11): p. 3153-3163.

19. T. Matsoukas, and E. Gulari, Dynamics of growth of silica particles from ammoniacatalyzed hydrolysis of tetra-ethyl-orthosilicate. *Journal of Colloid and Interface Science*, 1988. 124(1): p. 252-261.

20. L Wang, L Tao, et al. Dehydrogenation and aromatization of methane under non-oxidizing conditions. *Catalysis Letters*. 1993, Volume 21, Issue 1-2, p. 35-41.

21. Hirschfelder, Curtiss and Bird (1954) Molecular Theory of Gases and Liquids, Wiley, New York.

22. T Zhang, Michael D. Amiridis. Hydrogen production via the direct cracking of methane over silica-supported nickel catalysts. *Applied Catalysis A*: *General* 167 (1998): p. 161-172.

23. R Aiello, J. E. Fiscus et al. Hydrogen production via the direct cracking of methane over Ni/SiO2: catalyst deactivation and regeneration. *Applied Catalysis A: General* 192 (2000): p. 227-234.

24. Rahul D. Solunke and G Veser. Hydrogen Production via Chemical Looping Steam Reforming in a Periodically Operated Fixed-Bed Reactor. *Ind. Eng. Chem. Res*. 2010, 49, p. 11037-11044.

25. J. J. Spivey, G. Hutchings. Catalytic aromatization of methane. *Chem. Soc. Rev.*, 2014, 43, p. 792-803.

26. K Skutil, M Taniewsk. Some technological aspects of methane aromatization (direct and via oxidative coupling). *Fuel Processing Technology* 87 (2006): p. 511-521.

27. J Adanez, de Diego LF, F Garcia-Labiano, P Gayan, A Abad, JM Palacios. Selection of oxygen carriers for chemical-looping combustion. *Energy Fuels* 2004 18: p. 371-377.

28. S Bhavsar, B Tackett, G Veser. Evaluation of iron- and manganese-based mono- and mixed-metallic oxygen carriers for chemical looping combustion. *Fuel* 136 (2014): p. 268-279.

29. Jungho Jae, Geoffrey A. Tompsett, Andrew J, et al. FosterInvestigation into the shape selectivity of zeolite catalysts for biomass conversion. *Journal of Catalysis*. 279 (2011): p. 257-268.

30. Y Xu, S Liu, L Wang, et al. Methane activation without using oxidants over Mo/HZSM-5 zeolite catalysts. *Catalysis Letters.* 30 (1995): p. 135-149.

31. S Liu, L Wang, R Ohnishi, and M Ichikawa. Bifunctional Catalysis of Mo/HZSM-5 in the Dehydroaromatization of Methane to Benzene and Naphthalene XAFS/TG/DTA/ MASS/FTIR Characterization and Supporting Effects. *Journal of Catalysis* 181 (1999): p. 175–188.

32. B Monnerat, L Kiwi-Minsker, A Renken. Hydrogen production by catalytic cracking of methane over nickel gauze under periodic reactor operation. *Chemical Engineering Science.* 56 (2001): p. 633-639.